Material Reconstruction in X-ray Imaging

Der Naturwissenschaftlichen Fakultät
der Friedrich-Alexander-Universität Erlangen-Nürnberg
zur Erlangung des Doktorgrades

vorgelegt von
Markus Firsching
aus Bad Neustadt/Saale

Als Dissertation genehmigt von der Naturwissenschaftlichen Fakultät
der Universität Erlangen-Nürnberg

Tag der mündlichen Prüfung:	05. März 2009
Vorsitzender der Promotionskommission:	Prof. Dr. Eberhard Bänsch
Erstberichterstatter:	Prof. Dr. Gisela Anton
Zweitberichterstatter:	Prof. Dr. Christian Stegmann

Für Karo

Contents

List of Figures

List of Tables

Introduction

Motivation

For over a century, X-rays have been used for imaging. They provide a non-invasive and easy visual access inside the human body. Even with new competing technologies it has not lost much of its importance. But it is, of course, linked to an undesirable radiation exposure. X-rays used in medical diagnosis are the major source of exposure to human-made radiation in the industrialised counties. Therefore the radiation dose necessary for medial imaging should be reduced as much as possible without worsening the image quality.

To achieve this goal, it is mandatory to use all available information for imaging. Due to the quantisation of electromagnetic radiation, it is logical that the maximum of information for static imaging is gained when both energy and position of an X-ray photon are measured behind the patient. With a high photon flux of up to 10^{10} photons $s^{-1}cm^{-2}$ required in medical X-ray imaging, conventional detector concepts are either limited by the count rate or do not provide spectral information. Thus, the approach for X-ray imaging with respect to photon energy was so far made by highly customised source spectra only.

Detector Technology

Most detectors currently used are working in an energy integrating mode, i. e. they integrate the energy deposition of all photons in the sensor pixel over the complete acquisition time. Information on the photon energy is only available if exactly one photon is detected and processed one after the other.

The newest generation of detectors for (medical) X-ray imaging are working in a photon counting mode. These detectors are capable of detecting single photons even at the required rate for medical imaging and can still offer information about the photon energy. An example for such a detector is the Medipix2 which is employed in this work. It consists of two layers: A semiconductor layer to convert the photons to electron-hole pairs and an electronic layer where the signal of the generated charge carriers is processed and the absorbed photons are counted. Adjustable energy thresholds for counting the photons allows the access to spectral information. A more detailed description of the detector can be found in chapter 1.2.

Aim

The goal of this thesis is to develop and implement a new method to distinguish different materials in X-ray imaging, using the energy resolving capabilities of the Medipix2. The method is based upon the different energy dependence of the X-ray attenuation of the involved materials. It offers a new imaging modality and quantitatively reconstructs the concentrations of the respective materials in both radiography and computed tomography (CT). This material selectivity allows to enhance the image quality without additional radiation dose.

Potential Applications of Material Reconstruction

The method of material reconstruction can be used in medical X-ray imaging. It is of special value when used in combination with contrast agents. Such contrast agents increase the attenuation wherever they are located and help to visualise structures otherwise being very low in contrast or even invisible at all. Contrast agents usually contain a heavy, i e. high Z element, such as iodine, barium or gadolinium. In some applications it is beneficial to be able to distinguish the contrast agent from other high absorption structures as bones or calcifications. In conventional X-ray imaging it is then necessary to take two acquisitions, one with and one without the contrast agent, which effectively doubles the radiation dose. At this point, using a spectroscopic detector allows a technique as material reconstruction. It can deliver the concentrations of the contrast agent and other materials by exploiting the differences in their X-ray attenuation spectra.

Another application of material reconstruction is in material science, especially in non-destructive testing. It can be used for many applications of X-ray imaging, where the concentration of different components in a compound material is of interest.

Structure of this Thesis

This thesis is divided into three parts: basics, methodology and measurements and results. The first part starts with an introduction to photon counting detectors and their spectral resolution abilities. It is followed by a chapter giving a short presentation of computed tomography.

The second part introduces the employed tools and the developed methods to realise the material reconstruction technique. It starts with a description of the utilised Monte Carlo simulation and its extension to allow the simulation of the spectroscopic behaviour of the Medipix2 detector. The fourth chapter is attended

to the spectrum reconstruction technique. With the knowledge of the spectroscopic detector response from the simulation, the technique allows the reconstruction of the incident spectrum. Together, the simulation of the spectroscopic behaviour of the Medipix2 and the feasibility of the spectrum reconstruction provide the basis for material reconstruction. In the fifth chapter, the actual material reconstruction method is presented. It includes a presentation of the underlying physical model and different implementations of the method. The last chapter of this part introduces a method call enlarged field of view method. It allows multiple small detectors to be used for Computed Tomography in fan beam geometry without the need of seamless tiling.

In the third part, the measurements and results are presented. The seventh chapter describes the experimental setup including the employed X-ray source and the periphery needed for data acquisition. In the next chapter, both measurement and simulation results for the enlarged field of view method are shown and discussed. The detector energy response of the Medipix2 is dealt with in the ninth chapter. Measurements with monochromatic radiation as well as Monte Carlo simulations are presented and compared. The spectrum reconstruction method basing upon the detector response is presented in the subsequent chapter. Thereafter the application of material reconstruction is demonstrated in the twelfth chapter, both in radiography and computed tomography. At the end of the thesis, a summary is given.

Part I

Basics

1 Photon Counting X-ray Detectors

1.1 The Concept of Photon Counting

In the recent past, a new type of pixelated solid state X-ray detectors featuring the single photon counting concept were established. These photon counting detectors usually have a structured semiconductor layer where photons interact and generate electron-hole pairs. The charge carriers are drifting to the electrodes in an applied electric field. One side of the sensor layer is bonded to the electronic layer, feeding the signal into the pixel electronics where it is counted.

As the X-ray field is quantised itself, the most information is gained, if the photons are registered and processed individually. The integration density of electronic components that is possible nowadays allows to equip every pixel with complex electronics typically comprising a charge sensitive preamplifier, a discriminator with an adjustable threshold to suppress dark noise and a counter. That way, practically unlimited acquisition times are possible. Multiple thresholds and counters or multiple measurements at different threshold values introduce energy resolving capabilities. Very good linearity is provided until the flux is so high that the preamplifier signal has no time to return below the discriminator threshold, the so-called pile up. Aside from this limitation at very high flux, the dynamic range is only limited by the counter depth.

A number of photon counting detectors have been developed in the past, partly in an experimental stage.

DIXI is developed at the University of Uppsala. The square pixels have a side length of 270 µm [EBB+04]. It has 31×32 pixels resulting in an area of $0.723\,\mathrm{cm}^2$. A distinctive feature of the detector is the double counter in every single pixel, which allows two consecutive acquisitions within a short period of time.

PILATUS is developed at the Swiss Light Source (SLS) in Villingen. The detector has a size of $8.4 \times 3.3\,\mathrm{cm}^2$ and a pixel size of $172\,\mu\mathrm{m}^2$ [SBE+04]. An other version of the Pilatus detector has $217\,\mu\mathrm{m}^2$ pixel size and allows the tiling of multiple detectors to an area up to $40 \times 40\,\mathrm{cm}^2$ with a total of $2k \times 2k$ pixels [BBD+08]. It comprises a single discriminator and a 15-bit counter.

XPAD is developed at the ESRF in Grenoble. The project has already reached the third generation of detectors and has a matrix of 80 × 120 pixels each of 130 µm × 130 µm [PBB+07]. The current version has two discriminator thresholds allowing the operation in an energy window mode, counting only the photons with an energy within that energy range.

MPEC development started in 1997 at the University of Bonn [FHO+98]. The detector has 32×32 pixels with a pixel size of 200×200 µm^2. This version 2.3 of this detector is also built with cadmium telluride as sensor material [LFK+04].

To exemplify the setup and functionality of such a pixel detector, the Medipix detectors will be described in more detail.

1.2 The Medipix Detectors

In the early 1990s, the Medipix1 collaboration [Med] was established and the Medipix1 detector was developed and presented in 1997 [CHM+98]. It was followed by a whole family of detectors. This work will focus on the second member of this family, the Medipix2 [LCD+02]. It has 256 × 256 square pixels of 55 µm side length resulting in a total sensitive area of 1.98 cm^2. Different versions have been developed; in this work the Medipix2 and the enhanced version called Medipix2-MXR featuring an improved temperature stability and finer threshold adjustment were used. The Medipix2 is three-side buttable, allowing the tiling of a $2 \times n$ -array of detectors. The existing 2 × 2 -array of Medipix2-ASICs called Medipix2-quad has an area of 8.05 cm^2.

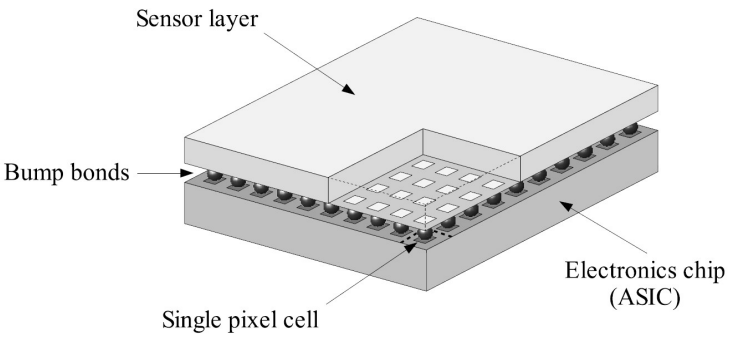

Figure 1.1 Hybrid flip-chip design: every pixel is bump-bonded to its pixel electronics [Pfe04]. Not to scale.

The Medipix detectors are hybrid detectors, i. e. they consist of a pixelated semiconductor sensor layer and the CMOS (**C**omplementary **M**etal **O**xide **S**emiconductor) ASIC (**A**pplication **S**pecific **I**ntegrated **C**ircuit) containing the pixel electronics and readout interface. The sensor layer is designed as a top to bottom pin-diode which is reverse biased to or beyond full depletion. Every pixel has a charge sensitive preamplifier and one or more adjustable discriminator thresholds. The Medipix2 has two discriminators creating an effective energy window, as they inhibit a signal to be counted if it is above the high threshold or below the low threshold and one 14-bit counter per pixel. In this work, both "energy threshold" and "threshold" refer to the lower thresholds unless otherwise noted. A very detailed description of the Medipix2-ASIC and its functionality can be found in Llopart's Ph. D. thesis [Llo07]. The upcoming Medipix3 [BCH+07] is manufactured in an 8-metal 0.13 µm CMOS technology and offers additional functionality per pixel as increased energy resolution and two 15-bit counters per pixel. It provides the possibility to connect a sensor with half the pixel pitch of the electronic pixels, resulting in a sensor pixel area four times larger than one electronic pixel. Furthermore, it allows to use the counters and discriminator thresholds of four electronic pixels with one sensor pixel. In that case, the resulting pixel matrix is 128×128 pixels with the size doubled to 110 μm^2

Figure 1.1 shows a schematic view of the sensor layer flip-chip bonded to the ASIC using lead-tin or indium bond beads. This layout allows the independent development and higher flexibility of both parts, e. g. the use of different sensor materials and thicknesses.

1.3 Energy Response

1.3.1 Interaction of Photons in the Sensor Layer

For photon counting detectors like the Medipix2, the sensor serves as a direct converting system: an incoming photon interacts with the sensor material, energy is transferred to the kinetic energy of an electron through Compton scattering or photo effect[1]. In the second step, the electron propagates through the semiconductor and loses kinetic energy while generating electron-hole pairs and phonons. Unfortunately, photo effect and Compton scattering result in subsequent photons which may reach into another pixel or escape from the detector. In the case of Compton scattering, only a fraction of the energy of the primary photon is transferred to the electron.

[1] As only photon energies well below 1 MeV are considered here, pair production is neglected.

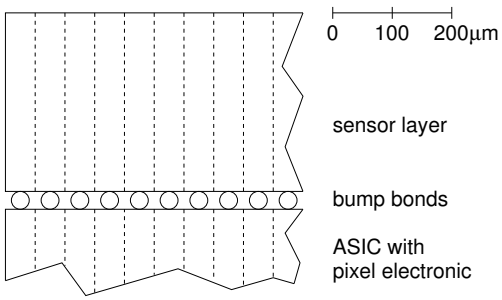

Figure 1.2 Scale drawing of a cut through the Medipix2 with a 300 µm thick sensor layer. The large aspect ratio between sensor thickness and pixel size can be seen. The 700 µm ASIC is cropped.

The maximum energy transfer occurs at a scattering angle of 180° and is given by

$$E_{\max} = \frac{2E^2}{m_e c^2 + 2E} \tag{1.1}$$

where E is the primary photon energy and m_e the electron mass. In case of photo electric absorption, the fluorescence photon has smaller energy than the incident photon. Thus, the energy deposition of an interaction in the sensor layer may be different to the primary photon energy.

1.3.2 Propagation of the Charge Carriers in the Sensor

The number of generated electron hole pairs is a measure of the transferred energy but is subject to statistical fluctuations. The ratio of these fluctuations to the fluctuations expected by Poisson statistics is called Fano factor [Fan47]. Electrons and holes are drifting to their respective electrodes in the applied electric field. Both repulsion and diffusion during drift cause a broadening of the charge carrier distribution. According to Spieler and Haller [SH85], the lateral diffusion can be described as a normal distribution with a standard deviation σ_T in the electrode plane depending only on the depth of interaction above the electrode z and the constant electrical field strength E:

$$\sigma_T \propto \sqrt{\frac{z}{E}} \tag{1.2}$$

Additionally, scattered photons or subsequent fluorescence photons may interact again at a different location, so single photons can trigger multiple events and more than one pixel can actually produce a signal from one photon. Together, these effects

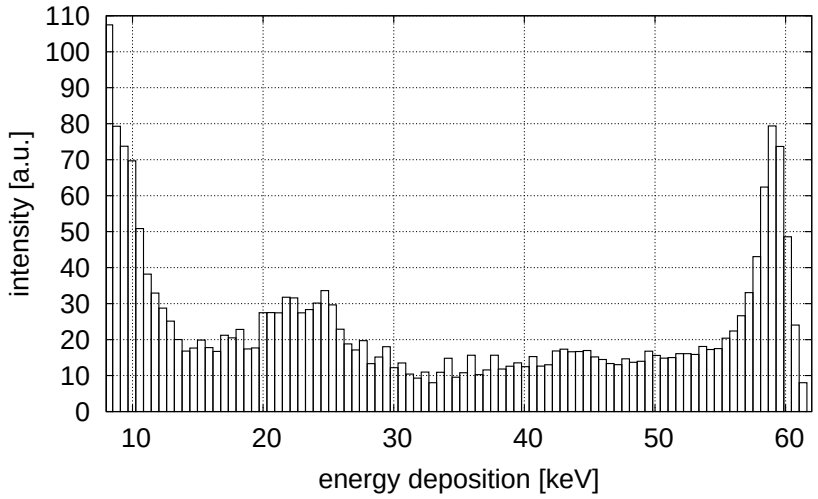

Figure 1.3 The differentiated threshold scan shows the measured energy response function of a Medipix2 detector with 300 µm Si sensor to mono-energetic irradiation at an energy of 59.3 keV, thus it corresponds to $R(E', 59.3\,\text{keV})$. The photo peak at primary energy (59.3 keV), Compton edge at 11 keV and fluorescences of parts of the detector assembly are clearly visible.

are called charge sharing, because the generated charge can be distributed between several pixels.

A scaled drawing of a cross section through the Medipix2 with a 300 µm thick sensor layer can be seen in figure 1.2. It shows the large aspect ratio between the sensor thickness and the pixel pitch, which eases the charge sharing between pixels through drift.

1.3.3 Energy Response of the Medipix2 Detector

Charge sharing strongly influences the energy response of the detector, which results in a broad contribution at all energies below the primary photon energy. This contribution originates from the distribution of the charge carriers during their generation and drift towards the electrodes. At small pixel sizes it is likely that a considerable fraction of the charge carriers reach into a neighboring pixel. The charge which is the measure for the energy deposition, is shared between pixels and therefore leads to an altered energy response. As a consequence of the above mentioned effects and the inevitable additional electronic noise from the preamplifier, the energy response of the detector is broadened and has a characteristic structure.

Figure 1.3 shows the measured energy response of a Medipix2 detector to irradiation with 59.3 keV photons ($K_{\alpha 1}$ line of tungsten). It is obtained through a differentiated threshold scan, i. e. the energy threshold is increased successively after each acquisition frame. Afterwards it is differentiated with respect to the threshold energy resulting in the detected energy deposition spectrum.

The peak at the primary energy of 59.3 keV corresponds to photo-electric absorption. Its width mainly depends on the electronic noise of the ASIC. The peaks at 22 keV and 25 keV originate from fluorescences of silver and tin, both present in the detector assembly. Tin is present in the bump bonds and silver is present in the glue used to connect the ASIC to the PCB (**P**rinted **C**ircuit **B**oard).

At 59.3 keV photon energy, Compton scattering is the dominating effect in silicon. According to equation (1.1), the maximum energy transfer between photon and electron is 11.17 keV for 59.3 keV photon energy. Thus the edge around 11 keV visible in figure 1.3 is the Compton edge.

The detector response spectrum is a function of both the primary photon energy E and the energy deposition E' and will be called $R(E', E)$ here. It will be shown in chapter 9.2 that the response function $R(E', E)$ can be simulated using Monte Carlo methods with good agreement with the measurement. For the energy range in medical imaging between 10 keV and 150 keV it is therefore be assumed to be known. In the case of a polychromatic X-ray source, the measured spectrum is a superposition of the response functions to monochromatic irradiation $R(E', E)$, weighted with the incident spectrum $s(E)$:

$$m(E') = \int_0^\infty R(E', E) \cdot s(E) \, \mathrm{d}E \tag{1.3}$$

Figure 1.4 shows the spectrum $s(E)$ of an X-ray tube with Molybdenum anode at 40 kV with beryllium and aluminum filtering of 1 mm thickness each, calculated according to Boone's model [BFJ97]. Figure 1.5 shows the simulated response $m(E')$ of a Medipix detector with a 300 µm silicon sensor layer. The principle of this simulation is described in chapter 3 and the further results are presented in chapter 9. The difference between the incident spectrum and the simulation of the measurable spectrum is clearly visible. Charge sharing changes the shape of the spectrum and shifts it to lower energy deposition channels. In the example, the incident spectrum $s(E)$ (see figure 1.4) has negligible content below 12 keV. However, in the measured energy spectrum $m(E')$ (see figure 1.5), there are major contributions below 12 keV. The low absolute values for the energy deposition spectrum are due to the low efficiency of 300 µm silicon as detection material.

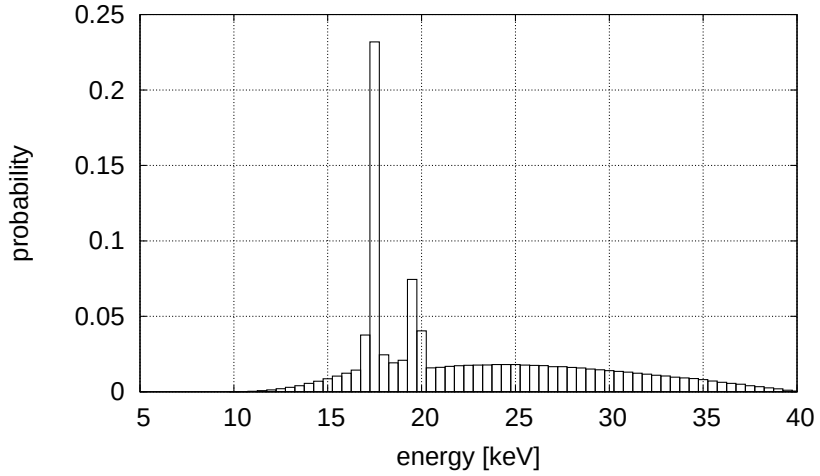

Figure 1.4 X-ray spectrum of an X-ray tube at 40 kV with molybdenum anode. This spectrum is referred to as $s(E)$ in the text. Clearly visible are the K_α- and K_β-lines at 17.4 keV and 19.6 keV. The spectrum was generated using Boone's model [BFJ97].

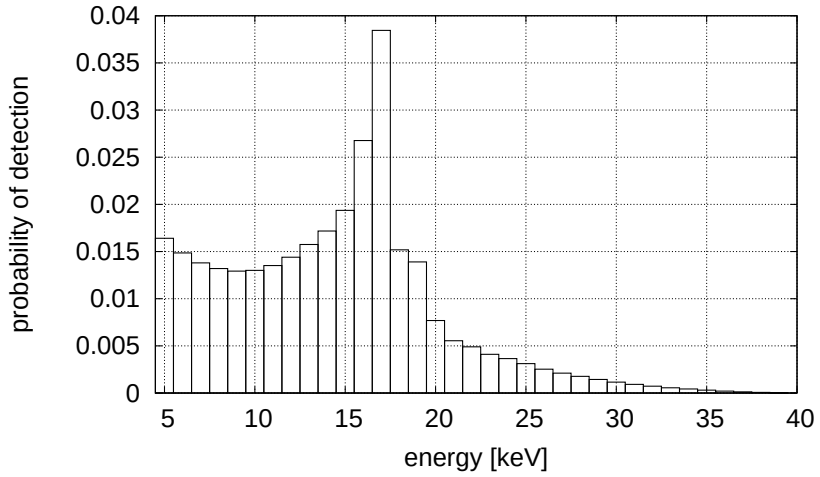

Figure 1.5 Monte-Carlo simulation of the Medipix2 response to the above 40 kV molybdenum spectrum with an energy bin size of 1 keV. This spectrum is referred to as $m(E')$ in the text. The spectrum differs considerably from the one in figure 1.4 due to charge sharing. Due to electronic noise, measurements below 5 keV are not possible.

2 Principles of Computed Tomography

2.1 History

A conventional X-ray image shows the projection of the object under investigation. Information about the depth of a structure inside the object cannot be accessed with conventional X-ray imaging. Computed tomography was the first technique to image the cross section of a closed object, rather than the projection.

The mathematical background of computed tomography, today known as "Radon transformation", was independently invented three times. It was first described 1917 by Johann Radon [Rad17] and barely noticed outside the mathematics communities. Without knowledge of Radon's work, Allan Cormack developed the mathematical framework and its application to radiology in 1963 [Cor63]. The first actual CT scanner was developed and built by Sir Godfrey Hounsfield in 1973 [Hou73], independently and without the knowledge of Radon's and Cormack's work. Cormack and Hounsfield shared the 1979 Nobel Prize for medicine and physiology.

In the beginning, computed tomography was very slow and had low spatial resolution. Featuring its great contribution to radiology, it was improved and established quickly. This new imaging method revolutionised medical diagnosis and lead to a new era of digital imaging. Today, there are thousands of the scanners installed worldwide and being used every day.

2.2 Radon Transform

Computed tomography is based on the attenuation of X-rays. The X-ray attenuation through an object is described by Lambert-Beer's law with the line integral along the beam over the spatial distribution of the attenuation coefficient $\mu(x, y)$. At a primary intensity I_0, the intensity behind the object is

$$I = I_0 \cdot \mathrm{e}^{-\int \mu \, \mathrm{d}s} \tag{2.1}$$

where s is the path through the object.

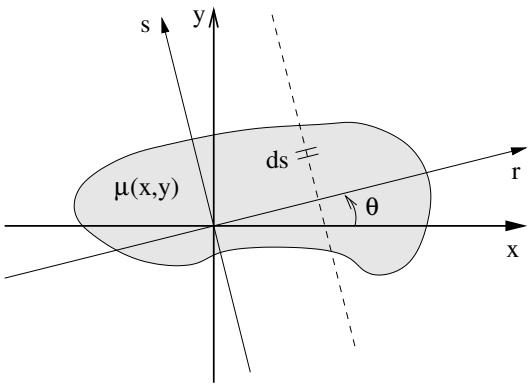

Figure 2.1 Computed tomography setup geometry

The integrated attenuation along s onto a perpendicular line r is called projection. In a CT scan, multiple projections p of the object angles θ [Opp05]:

$$p(r,\theta) = -\log \frac{I(r,\theta)}{I_0} = \int \mu(x,y)\,\mathrm{d}s \tag{2.2}$$

The transformation of the distribution of the attenuation coefficient μ to the rotated system leads to

$$p(r,\theta) = \int \mu(r\cos\theta - s\sin\theta, r\sin\theta + s\cos\theta)\,\mathrm{d}s \tag{2.3}$$

The entity of these projections form the Radon transform $\mathcal{R}[\mu]$ of the spatial distribution of the attenuation coefficients.

The two dimensional diagram of the projections p as a function of the rotation angle θ and the detection position[1] r is called sinogram. The sketch of the geometric setup for computed tomography is shown in figure 2.1.

2.3 Fourier Slice Theorem

To obtain the spatial distribution of the attenuation coefficient $\mu(x,y)$, it is formally sufficient to invert the radon transformation. This can be achieved with the help of the Fourier Slice Theorem (FST).

[1]The detection position (or the detector element at that position) is the distance between the beam and the centre of rotation.

Without loss of generality the projection along the y-axis is chosen:

$$p(r,\theta)\big|_{\theta=0} = p(x) = \int \mu(x,y)\mathrm{d}y \tag{2.4}$$

The two dimensional Fourier transform $\mathcal{F}_2$ of $\mu(x,y)$ is

$$M(k_x,k_y) = \int\int \mu(x,y)\,\mathrm{e}^{-i(xk_x+yk_y)}\,\mathrm{d}x\mathrm{d}y = \mathcal{F}_2\mu(x,y) \tag{2.5}$$

where k_x and k_y are the components of the spatial frequency. The slice $s(k)$ at $\theta = 0$ is then $M(k_x,0)$:

$$\begin{aligned} s(k)\big|_{\theta=0} = M(k_x,0) &= \int\int \mu(x,y)\,\mathrm{e}^{-ixk_x}\,\mathrm{d}x\mathrm{d}y & (2.6)\\ &= \int \left[\int \mu(x,y)\,\mathrm{d}y\right] \mathrm{e}^{-ixk_x}\mathrm{d}x \\ &= \int p(x)\,\mathrm{e}^{-ixk_x}\mathrm{d}x \quad = \quad P(k,\theta)\big|_{\theta=0} & (2.7)\end{aligned}$$

which is the one-dimensional (1-D) Fourier transform of projection $p(x)$, i. e. the FST states that the Fourier transform P of the projection p of the two-dimensional (2-D) function $\mu(x,y)$ onto a line r under the angle θ is equal to a slice $s(k)$ under the same angle through the origin of the 2-D Fourier transform M of $\mu(x,y)$.

In operator notation it can be written as

$$\mathcal{F}_1 p = \mathcal{F}_2\mu \tag{2.8}$$

where $\mathcal{F}_1$ is the 1-D and $\mathcal{F}_2$ the 2-D Fourier transformation.

Therefore, the inverse Radon transform can be achieved by the 1-D Fourier transform of the projections, which lead to the 2-D Fourier transform M of the attenuation coefficients μ. These can then be calculated by the inverse 2-D Fourier transform.

By the measurement of projection lines under certain angles, M is obtained in polar coordinates. Unfortunately, polar coordinates are not useful for numerical inversion as no efficient algorithm for discrete Fourier transform (as the Fast Fourier Transform (FFT) in Cartesian coordinates) in polar coordinates was known before the proposal of Averbuch et al. [ACD$^+$06]. This method has not been adopted yet for standard use in computed tomography.

2.4 Filtered Back Projection

Another approach to reconstruct the distribution of attenuation coefficients is the filtered back projection (FBP).

The back projection $\mathcal{B}$ of a projected function (in this case the distribution of the attenuation coefficient μ) is called b and defined as

$$b(x,y) = \int \mathcal{R}\mu(x\cos\theta + y\sin\theta, \theta)\,\mathrm{d}\theta \tag{2.9}$$

$$\text{or in operator notation} \quad = \mathcal{B}\mathcal{R}\mu = \mathcal{B}p \tag{2.10}$$

which means that all integration paths of the previous projection through a point are summed up in this point during back projection. Thus, every point of the original function contributes to all points weighted reciprocally with the distance r, i. e. it is convoluted with $\frac{1}{r}$:

$$b(x,y) = \mu(x,y) * \frac{1}{r} \tag{2.11}$$

Since a convolution is a multiplication in the Fourier space and the Fourier transform of $\frac{1}{r}$ is $\frac{1}{|k|}$ with spatial frequency k, the 2-D Fourier transform of equation (2.11) can be written as

$$\mathcal{F}_2 b(x,y) = \mathcal{F}_2\mu(x,y) \cdot \frac{1}{|k|} \tag{2.12}$$

Solving this equation for the attenuation coefficients μ in an algebraic notation leads to

$$\mu(x,y) = \mathcal{F}_2^{-1}\left[|k| \cdot \mathcal{F}_2 b(x,y)\right] = \mathcal{F}_2^{-1}\left[|k| \cdot \mathcal{F}_2\mathcal{B}p_\theta(r)\right] \tag{2.13}$$

$$= (\mathcal{F}_2^{-1}|k|) * b(x,y) = h(r) * \mathcal{B}p_\theta(r) \tag{2.14}$$

where $\mathcal{F}_2^{-1}$ is the inverse 2-D Fourier transform. Thus, the original function can be represented as a convolution of the back projection with a filter kernel $h(r) = \mathcal{F}_2^{-1}|k|$. For efficiency reasons, it is beneficial to permute the Fourier transform with the back projection in (2.13) and apply the Fourier slice theorem. In this case, only 1-D Fourier transformations are needed:

$$\mu(x,y) = \mathcal{B}\Big[\mathcal{F}_1^{-1}\left[|k| \cdot \mathcal{F}_1^{-1}p_\theta(r)\right]\Big] \tag{2.15}$$

Instead of the linear ramp filter $|k|$, special filter functions can be used to achieve certain goals like smoothing, by reducing the filter function at higher spatial frequencies, or sharpening, by increasing it.

Part II

Methodology

3 The Simulation Tool ROSI

3.1 Reasons for Using Monte Carlo Simulations

Monte Carlo simulations are a powerful tool and have been used in research for many years. They allow to evaluate a virtual setup without needing to build it in reality and can help to understand complex experimental setups as they provide full control over all parameters. In case of an X-ray imaging setup, it is possible to estimate the influence of scattered radiation of the object. Furthermore, the it allows a comparison between an ideal and the real detector.

3.2 The Basic ROSI Package

The Monte Carlo simulations in this work were done with ROSI[1] [Gie04, GD08]. It is an object orientated X-ray simulation tool [Gie02, GWA03]. It was developed at the institute of physics, FAU Erlangen-Nürnberg and is published under the GNU General Public License (GPL) [Fou91]. ROSI has an easy to use interface and comes with a large database of materials, including all natural elements and a variety of tissues according to the ICRU reports 44 and 46 [ICR89, ICR92].

ROSI simulates the transport of particles as photons or electrons through matter on an event basis. The interactions of the particles and their possible subsequent daughter particles are stored in a tree structure to provide easy access. The geometry and physics are combined in the library LSCAT-GISMO [ABB+93, GWA04] with the three physics classes that can be found in tab. 3.1.

name	function
Gheisha	hadronic interactions
EGS4 [NHR85]	electromagnetic interactions
LSCAT [NH00]	low energy extension to EGS4

Table 3.1 Parts of LSCAT-GISMO

EGS4 (**E**lectron **G**amma **S**hower) is a widely used package for the simulation of the coupled transport of electrons and photons.

[1] ROSI is an acronym for **RO**entgen **SI**mulation, German for "X-ray simulation".

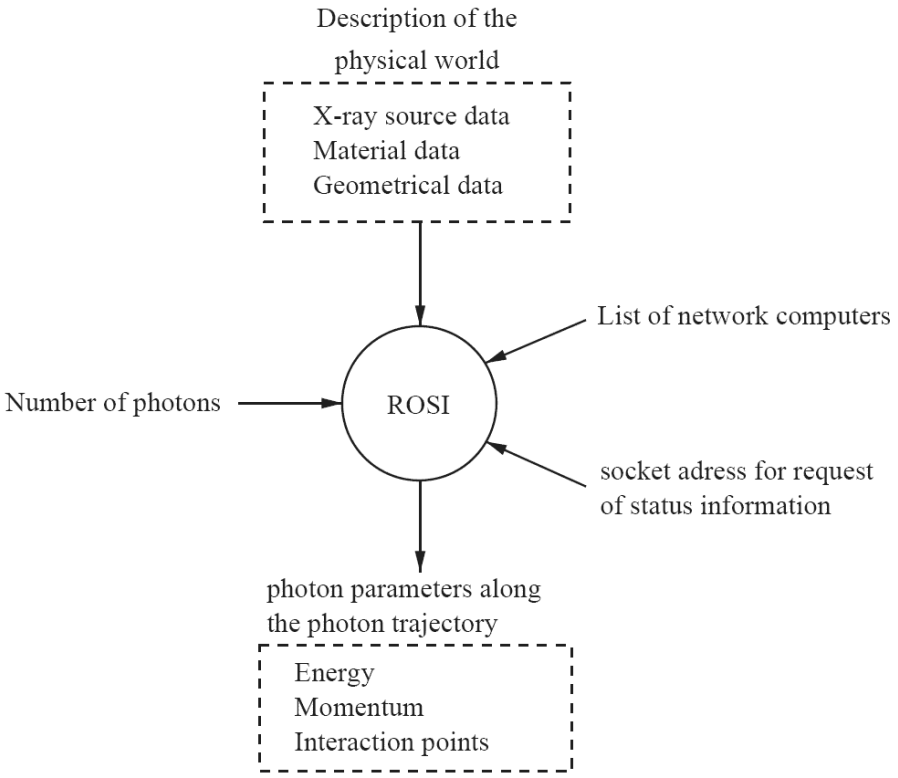

Figure 3.1 Black box model of ROSI [GWA03]

Random numbers are provided by the object orientated class library RAVAR (**RA**ndom **VAR**iable) which is part of ROSI. RAVAR and LSCAT-GISMO use the random number generator algorithm after James [Jam90] with a seed from the interval [0, 900 000 000] and a period length of approximately 10^{34}.

Every photon and its interactions are processed independently in the simulation. Therefore, the number of photons to be simulated can be split into smaller work packages which are distributed to multiple computers. ROSI can do that automatically using the MPI/LAM (**M**essage **P**assing **I**nterface / **L**ocal **A**rea **M**ulticomputer) environment [BDV94] in a TCP/IP (**T**ransmission **C**ontrol **P**rotocol / **I**nternet **P**rotocol) network.

ROSI provides a user-friendly yet flexible implementation of X-ray sources, detectors and all kinds of geometric objects in the simulation world. Furthermore it allows easy access to the event tree, where all information is stored. Figure 3.1 shows a black box model of the simulation programme. A more detailed description of ROSI can be found in the appendix A of Durst's PhD thesis [Dur08].

3.3 Extension of the Simulation

The standard programme of ROSI was extended to take into account the pixelated structure and the behavior of the electron hole pairs in the semiconductor sensor layer. This extension allows the simulation of the charge sharing between pixels. The developments took place in cooperation with Alexander Korn, Björn Kreisler and Jürgen Durst within the novel detector group at the institute of physics, FAU Erlangen-Nürnberg in Erlangen.

3.3.1 Implementation of the Geometric Structure

Information about the energy loss of charged particles during their track through the detector is supplied by the simulation. This information is collected after every incoming photon and assigned to the spatially corresponding pixel. Through this step, the contribution of charge sharing by fluorescence photons and Compton scattering is taken into account.

Aside from the silicon sensor layer, other structures of the detector assembly were implemented, as they cause back scattering and fluorescence photons. In detail, these are ASIC, bump bond beads and a layer of silver. The bump bond beads made from a lead-tin alloy are placed directly underneath the sensor layer and are implemented as cubes with 16 µm side length. The silicon ASIC is 700 µm thick. A thin silver layer is representing the silver contained in the glue that is used to contact the ASIC to the PCB. Especially the elements with high atomic number as lead, tin and silver contribute to fluorescence radiation in the detector setup. The remaining structures show very little effect and were neglected in the simulations.

3.3.2 Implementation of the Generation and Propagation of Charge Carriers

In the second stage of the extension, properties of the charge carriers in the semiconductor are considered. Both the generation and the propagation of the charge carriers are taken into account.

As described above, the energy deposition in the sensor layer per pixel per photon is collected in the first stage. This energy is converted to a corresponding number of electron hole pairs by dividing the energy deposition by the pair creation energy ϵ. These electron hole pairs are distributed equally between the two steps of the discretised CSDA (**C**ontinous **S**lowing **D**own **A**pproximation) used in the simulation. Photon energies in the range of 10 to 150 keV lead to energy depositions in the same order of magnitude. With silicon as sensor material ($\epsilon = 3.63\,\mathrm{eV}$) this

leads to at least thousands of electron hole pairs. The Fano factor for silicon is approximately 11.5% [ABS80]. This means that the production process of the charge carriers has a statistical fluctuation of only 11.5% of the root mean square (RMS) of the corresponding Poisson distribution. The noise contribution due to the Fano factor is small compared to noise contribution from the pixel electronics and was not taken into account in the simulation. For example, an energy deposition of 36.3 keV results in a mean number of 10,000 electron hole pairs, leading to a variation of approximately 12 electrons due to the Fano factor. For comparison, the electronic noise is approximately 140 electrons for the Medipix2 and 70 electrons for the Medipix2MXR.

Depending on the depth of generation, the drift time for every charge carrier is computed. To be able to do that, the electric field needs to be known. This is trivial for a plate capacitor, but for the structured sensor layer it is more difficult and is most suitably obtained by a finite element method. From that, the actual drift time is calculated and written to a look-up table. A detailed description of this technique can be found in [Kre06] and [Kor07].

With the help of that look-up table, the effective range for repulsion and diffusion can be calculated and the charge carriers are distributed accordingly. They are assigned to the corresponding pixels by their position and added for each pixel. If the energy deposition, i. e. the number of generated charge carriers, resulting from one impinging photon in a pixel is above a given threshold, the counter of this pixel is incremented by one.

This technique allows the exact simulation of the photon detection properties of a photon counting device. Measurements to corroborate the accuracy of the simulation are shown in chapter 9.

4 Spectrum Reconstruction

The energy response properties of the Medipix2 described in section 1.3 complicate the interpretation of the spectral information gained. However, the method of material reconstruction relies on the knowledge of the unbiased spectrum. Thus it is necessary to correct for the distortion in the energy response in order to get quantitative and precise information about the spectrum incident on the detector. A method to reconstruct the incident spectrum was developed.

4.1 Physical Model

The incident spectrum $s(E)$ is a function of the primary photon energy E. The detector response depends on that primary energy and is a function of the energy deposition E' per pixel of the detector. For monochrome impinging radiation, i. e. a Dirac function in energy, the overall spectral response can either be measured or simulated by sampling by a Dirac comb. One approach of using a relatively simple model for the spectral response is presented by Ponchut [Pon08]. For silicon used as sensor material, it is assumed there that the spectral response consists of just a primary peak and a plateau due to charge sharing, while the effects resulting from back-scattering and fluorescences are neglected. This is a good approximation only for energies smaller than 25 keV and relatively high threshold energies, but not applicable for higher primary photon energies. In contrast to this approach, the simulation of the complete detector assembly as described in the previous chapter provides the very accurate spectral response over a wide range of energies. Details to the spectral detector response can be found in chapter 9 of this work.

The entity of the spectral responses to monochrome radiation form the detector response $R(E', E)$[1]. The normalised form is the differential probability that a photon of the energy E leads to the energy deposition E'. With an impinging spectrum $s(E)$, the spectrum directly accessible with the detector is then $m(E')$:

$$m(E') = \int_0^\infty R(E', E) \cdot s(E) \, \mathrm{d}E \tag{4.1}$$

[1] In this context, the lower case letter is used for functions of one variable and for vectors (in the case of discrete notation), while the upper case is used for functions of two variables and matrices.

In a discrete notation, the energy deposition E' can be divided in N energy channels with index i, the primary photon energy in J channels with index j. The resulting $N \times J$ matrix R_{ij} is the linear transformation from the incident spectrum to the spectrum measurable with the detector:

$$m_i = \sum_{j=1}^{J} R_{ij}\, s_j \tag{4.2}$$

$$\mathbf{m} = \mathbf{R} \cdot \mathbf{s} \tag{4.3}$$

This system can be solved directly if R is square and has full rank, i. e. $\det(R) \neq 0$, and it is usually overdetermined if $N > J$. Since the response spectrum changes continuously with the primary energy, only a limited number of $J_{\max}$ energy channels can be considered to be linear independent beyond noise due to statistical fluctuations. This number is dependent on photon statistics, covered energy range and detector characteristics like energy resolution. In the energy range typically used for X-ray imaging (10–150 keV) with an energy bin size of few keV and using the Medipix2, $J_{\max}$ is around 30–40.

If $\mathbf{R}$ is square, it is an upper triangular matrix due to the fact that the energy deposition cannot exceed the primary photon energy. For the same reason, if $N \neq J$ and the binning for energy deposition and primary energy are different, the next higher energy deposition channel to the corresponding primary energy channel must also be zero. However, for small energy channels with an energy broadness in the same order of magnitude as the detector noise, it is possible that some photons may be registered above the primary energy due to various effects like Fano factor, threshold noise or amplifier noise.

The number of channels in the energy deposition domain N is limited only by the measurement. Since the threshold is realised as a digital-to-analogue converter (DAC) this is the step size of the DAC used. At typical settings, it is approximately 0.6 keV for the Medipix2 and approximately 0.15 keV for the Medipix2 MXR.

Provided that the response function for the detector is known, the incident spectrum can be recovered from the one measured with the detector. There are two different possibilities to do that, applying the pseudo inverse of the matrix $\mathbf{R}$ or the spectrum stripping method.

4.2 Matrix Inversion

Under the above mentioned constraints, the set of linear equations (4.2) can be solved. A particularly important constraint is the significant linear independence of the columns of $\mathbf{R}$, i. e. the detector energy responses to mono-energetic irradiation. The "hard" mathematical expression for linear independence, the determinant of R respectively $R^T R$, will remain non-zero due to statistical noise. Thus for significant linear independence in this case it is not sufficient for the determinant to be non-zero, but its absolute value must be greater than or equal to a numerical value $\epsilon > 0$. It means that the detector responses, which are assumed to be known, of neighboring primary energy channels differ well above statistical noise.

In case $\mathbf{R}$ is square, the solution is simply the inverse and the incident spectrum can be gained through

$$\mathbf{R}^{-1} \cdot \mathbf{m} = \mathbf{s} \tag{4.4}$$

If $N > J$, the pseudo inverse $\mathbf{R}^+$ can be applied. For linear independent columns of $\mathbf{R}$, i. e. if $\det(\mathbf{R}^T\mathbf{R}) > \epsilon$, it is $(\mathbf{R}^T\mathbf{R})^{-1}\mathbf{R}^T$:

$$\mathbf{R}^+ \cdot \mathbf{m} = (\mathbf{R}^T\mathbf{R})^{-1}\mathbf{R}^T \cdot \mathbf{m} = \hat{\mathbf{s}} \tag{4.5}$$

In this case $\hat{\mathbf{s}}$ is the best estimation for the spectrum in a maximum likelihood sense and is equivalent to a linear least squares fit [BL98]. This method works only with sufficiently large number of photons so that the statistical fluctuations are small. In practice, the number of detected photons must be a least serveral thousand.

4.3 Spectrum Stripping

Spectrum stripping is the successive subtraction of the respective energy response function from the measured spectrum. It starts at the highest energy deposition channel of the measurement with a non-zero entry. Then the detector response spectrum to monoenergetic irradiation corresponding to this highest energy channel is multiplied by a weighting factor and subtracted from the measured spectrum. The factor is chosen so that the result of the channel with the highest energy is zero after the first subtraction. This rule is applied recursively to the next non-zero channel until all channels are zero. The weighting factors now represent the reconstructed spectrum. The following example will depict the method.

As $\mathbf{R}$ is an upper triangular matrix for $N = J = 3$, equation (4.2) can be written as:

$$m_1 = R_{11}\,s_1 + R_{12}\,s_2 + R_{13}\,s_3 \tag{4.6}$$
$$m_2 = 0 + R_{22}\,s_2 + R_{23}\,s_3 \tag{4.7}$$
$$m_3 = 0 + 0 + R_{33}\,s_3 \tag{4.8}$$

Let m_3 be the highest non-zero measurement channel. The unknown factor is now $s_3 = m_3/R_{33}$, as this reduces m_3 to zero after the first subtraction:

$$m'_3 = m_3 - R_{33}s_3 = 0 \tag{4.9}$$
$$m'_2 = m_2 - R_{23}s_3 \tag{4.10}$$
$$m'_1 = m_1 - R_{13}s_3 \tag{4.11}$$

Now m'_2 is the highest non-zero channel and the factor to reduce it to zero by the subtraction is $s_2 = m'_2/R_{22} = (m_2 - R_{23}s_3)/R_{22}$. After the second subtraction the system looks as follows:

$$m''_3 = m'_3 = 0 \tag{4.12}$$
$$m''_2 = m'_2 - R_{22}s_2 = 0 \tag{4.13}$$
$$m''_1 = m'_1 - R_{12}s_2 = m_1 - R_{13}s_3 - R_{12}s_2 \tag{4.14}$$

Thus the reconstructed intensity in one primary energy channel is the contribution of the corresponding deposition energy minus the contribution of the higher energy channels to that energy. In general, using the indices i with $1, \ldots, i, \ldots, N$ for all primary energy channels and n with $s+1, \ldots, n, \ldots, N$ for the channels above i, the intensity in the primary energy channel s_i can be written:

$$s_i = \frac{m_i - R_{iN}s_N - R_{i(N-1)}s_{(N-1)} - \ldots - R_{i(i+1)}s_{(i+1)}}{R_{ii}}$$
$$s_i = \frac{m_i - \sum_{n=s+1}^{N} R_{in}s_n}{R_{ii}} \tag{4.15}$$

The application of spectrum reconstrution using both matrix inversion and spectrum stripping is presented and discussed in chapter 10.

5 The Method of Material Reconstruction

In both radiography and computed tomography, the imaged value is the attenuation of X-rays by the object. In plain radiography, the measurand is the line integral of the attenuation coefficient of the beam through the object, while computed tomography (CT) reconstructs the attenuation coefficient itself[1]. These attenuation coefficients are not only material specific, but also energy dependent.

5.1 Technologies using the photon energy for imaging

Different methods depending on such special spectra have been developed to exploit the information on photon energy for X-ray imaging.

An early method is the dual energy method in computed tomography [KFS87]. It depends on the two major effects contributing to X-ray attenuation in the energy range of medical X-rays, Compton scattering and photo electric effect. The photo electric effect is strongly depending on energy, while Compton scattering hardly depends on energy. The data is taken with two different, but known X-ray spectra. Through a parameterisation, the decomposed images of photo effect and Compton effect can be obtained, resulting in images emphasising bone and soft tissue contrast respectively.

Principal Component Analysis (PCA) has been applied to multi-energy X-ray computed tomography of mineral samples by Kalukin et al. [KVS00]. PCA is a method to maximise the variance of the data through a change of basis, i. e. the set of measurements with different source spectra In the case of imaging it is linked to a maximisation of the contrast between different materials. However, no additional information like the attenuation coefficients of the expected materials is used. Therefore the method can not provide quantitative material specific information.

A similar approach to the material reconstruction presented here has been performed by Menezes et al. [MSJ04]. They have employed a secondary target X-ray tube to generate a spectrum of multiple fluorescence lines. This material recognition technique is based on ratios of the attenuation coefficients of the respective material. However, the technique is not feasible for medical imaging, as intensity of the

[1] The unit commonly used in CT is the Hounsfield unit (HU), but this is also a measure for the attenuation coefficient μ as it is defined for a material x as $HU_x := 1000 \cdot \frac{\mu_x - \mu_{\mathrm{H2O}}}{\mu_{\mathrm{H2O}} - \mu_{\mathrm{air}}}$.

secondary target tube is very low. Furthermore, the technique is very sensitive to inaccuracies in the calibration.

All these techniques require special X-ray spectra. In contrast, acquiring the energy information on the detector side allows the usage of standard X-ray tube spectra which simplifies the application. In contrast, the basic idea of material reconstruction is to separate the object's components into different basis materials using an energy resolving detection.

5.2 Physical Model for Material Reconstruction

The mass attenuation coefficient $\mu'(E)$ of a compound material consisting of K basis materials (indexed k) is the sum of the mass attenuation coefficients of the components weighted with their respective mass ratio w_k:

$$\mu'(E) = \frac{\mu(E)}{\rho} = \sum_{k=1}^{K} w_k \mu'_k(E). \tag{5.1}$$

where ρ is the density.

The fraction of photons transmitting through the object is called transmittance T. According to Lambert-Beer's law, it is given by the exponential attenuation:

$$N(E) = N_0(E) \cdot T(E) = N_0(E) \cdot \mathrm{e}^{-\sum_k \mu'_k(E)\, a_k} \tag{5.2}$$

where N_0 is the number of incident photons, a_k is the areal density of the material component k and has the unit mass per area. These material components are called basis materials of the compound object. The areal density a_k is the projection of the density ρ of the k^{th} component along the X-ray path s:

$$a_k := \int \rho_k \, \mathrm{d}s. \tag{5.3}$$

Normalisation of N by division by N_0 and taking the negative logarithm leads to the new variable $t(E)$, the negative log-transmittance:

$$t(E) := -\ln T(E) = -\ln\left(\frac{N(E)}{N_0(E)}\right) = \sum_k \mu'_k(E)\, a_k \tag{5.4}$$

which is linear in the attenuation coefficients.

Written in terms of discrete energy channels, it is a set of linear equations (5.5) that can also be written in matrix notation (5.6):

$$t_j := -\ln\left(\frac{N_j}{N_{0j}}\right) = \sum_k \mu'_{jk}\, a_k \tag{5.5}$$

$$\mathbf{t} = \mathbf{M}\,\mathbf{a}. \tag{5.6}$$

The columns of the $J \times K$ matrix $\mathbf{M}$ are the energy dependent mass attenuation coefficients of the different basis materials. This set of linear equations is solvable for the areal densities $\mathbf{a}$ if the columns of $\mathbf{M}$ are linearly independent.

5.3 Choice of Basis Materials

The mass attenuation coefficients[2] of the constituents of a compound material form the basis for the total mass attenuation coefficient (see (5.1)). The material reconstruction method can only work if the basis materials are linearly independent with respect to their mass attenuation coefficient spectra, i. e. if the mass attenuation coefficient spectra of one basis material can not be represented by a linear combination of the remaining basis materials. However, their spectrum is usually not linearly independent for more than two components as the mass attenuation of X-rays only depends on two physical effects in the considered energy range, Compton scattering and photo electric absorption. Pair production cannot occur below 1.022 MeV and Rayleigh scattering was neglected as it is always dominated either by photo electric effect or Compton scattering in the considered energy range of 5-150 keV. Thus, the total mass attenuation coefficient can be written in good approximation as a linear combination of the mass attenuation coefficients originating only from photo electric ($\mu'_{\mathrm{pe}}(E)$) effect and Compton scattering ($\mu'_{\mathrm{cs}}(E)$):

$$\mu'(E) = \alpha \cdot \mu'_{\mathrm{pe}}(E) + \beta \cdot \mu'_{\mathrm{cs}}(E) \tag{5.7}$$

To illustrate the case of a linear dependence, figure 5.1 shows the mass attenuation coefficient of hydrogen, oxygen and calcium. Hydrogen with $Z = 1$ is dominated by Compton scattering, which is almost constant with respect to the energy in this range. Calcium ($Z = 20$) is dominated by photo electric absorption which has an energy dependence proportional to E^{-k} with $3 < k < 4$. The mass attenuation coefficient of oxygen ($Z = 8$) is dominated by photo electric absorption at the lower

[2] Mass attenuation and attenuation differ only by the density of the respective material, which is constant. Hence, for linear independence consideration, either could be used.

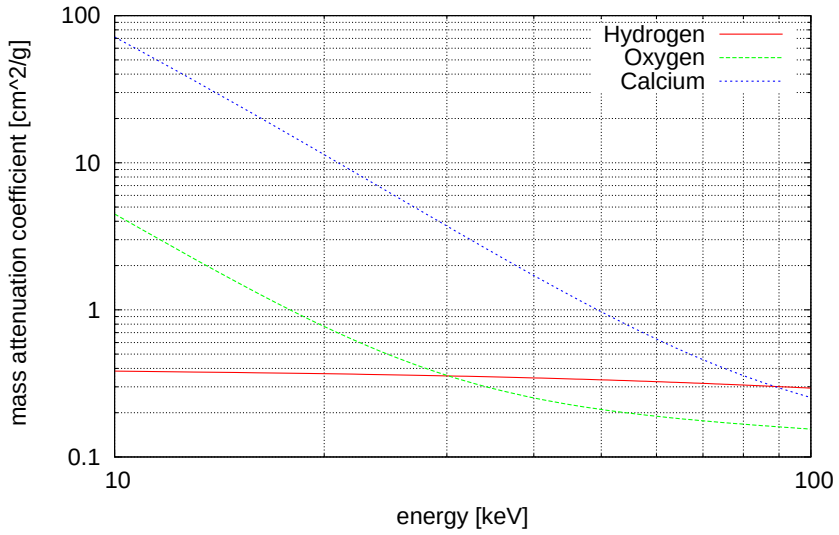

Figure 5.1 Mass attenuation coefficients of hydrogen, oxygen and calcium [BHea98]

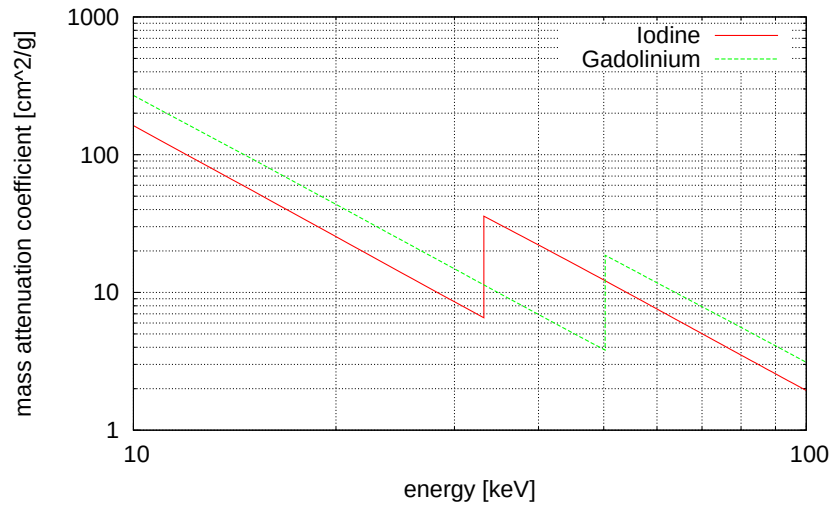

Figure 5.2 Mass attenuation coefficients of gadolinium and iodine

energies and by Compton scattering for the higher energies in this range. It can be represented as a linear combination of the mass attenuation coefficient of hydrogen and calcium. Therefore, these three materials could not be used as a set of basis materials for material reconstruction. Instead, hydrogen and calcium could be used as basis materials but the result would not longer provide the materials specific areal densities, as the contribution of oxygen to the total attenuation is distributed between the emloyed basis materials. With the same effect, the mass attenuation coefficients corresponding to photo electric absorption and Compton scattering can also be employed.

If more than two basis materials are desired for material reconstruction, materials with K-edges within the energy range can be employed to obtain linear independency. The K-edge is a very distinct property of the attenuation spectrum which cannot be obtained by a linear combination of the attenuation spectra of two other materials. The materials of choice with a K-edge in the favored energy range are iodine and gadolinium. Both of them are already used as contrast agents in medical imaging and licensed pharmaceuticals exist. The characteristic K-edges of the mass attenuation coefficients of iodine and gadolinium with their K-edges at 33.2 keV and 50 keV respectively can be seen in figure 5.2.

5.4 Different Implementations of Material Reconstruction

5.4.1 Pseudo Inversion

In the ideal case that the measurements are taken with J different discrete energies and an ideal energy resolving detector, the system can be solved using the (pseudo) inverse of that matrix $\mathbf{M}^+$.

$$\mathbf{M}^+ t = (\mathbf{M}^T\mathbf{M})^{-1}\mathbf{M}^T t = \hat{\mathbf{a}}. \tag{5.8}$$

However, this method can only be used in practice when combined with spectrum reconstruction and narrow energy bins.

This step is the actual transformation from the energy domain of the measurement to the material domain consisting of the amount of each basis material. In the case of (5.6) being over-determined, $\hat{\mathbf{a}}$ is the best estimation for $\mathbf{a}$.

5.4.2 Maximum Likelihood Approach

The likelihood function indicates how likely a particular set of parameters with known probability density function leads to an observed sample. Thus the maxi-

mum of this function is indicating the one set of parameters that have the highest probability to lead to the given measurement.

Provided the number of photons N_j (following Poisson statistics) in an energy channel j is high enough to be considered Gaussian distributed, the likelihood function for the number of photons in an energy channel is:

$$L(a_1, a_2, \ldots, a_k) = \prod_j \frac{1}{\sqrt{2\pi N_j}} \, \mathrm{e}^{-\frac{\left(N_j - N_{0,j} \exp(-\sum_k \mu'_{jk} a_k)\right)^2}{2N_j}}. \tag{5.9}$$

Since the logarithm is a continuous strictly increasing function over the range of the likelihood function, values maximising L will also maximise its logarithm $f := \ln(L)$ and minimise the negative $F := -f$. As most algorithms for extremal value search are performing the search for a minimum, the latter one will be used and the function to minimize is:

$$F(a_1, \ldots, a_k) = -\ln\left(L(a_1, \ldots, a_k)\right) = \text{const.} + \sum_j \frac{\left(N_j - N_{0,j} \, \mathrm{e}^{-\sum_k \mu'_{jk} a_k}\right)^2}{2N_j}. \tag{5.10}$$

This function is proportional to the sum of the squared differences between the estimate and the measurement. Minimising those differences therefore leads to the least squares method.

5.4.3 Method for Broad Incident X-ray Spectrum

Both methods introduced so far work only for a series of monochrome measurements. Access to monoenergetic radiation sources is complicated, especially for medical imaging. The material reconstruction method was adapted for use with broad energy spectra, for example spectra generated by an X-ray tube. When covering a broad range of energies with a limited number of energy bins, they can have significant width. In this case, the attenuation coefficients may change considerably, causing a beam hardening effect within an energy channel, i. e. the mass attenuation coefficients forming $\mathbf{M}$ cannot be assumed to be of constant value, but are also a function of the type and the amount of material the X-ray beam passes before.

For this reason, it is necessary to modify the physical model by introducing effective mass attenuation coefficients. The first component does not need to be corrected and for two components, only the second one needs the correction for this effect. The normalised effective transmittance within one energy channel ranging from E_1 to E_2 is then:

$$T_{\text{eff}} = \frac{\int_{E_1}^{E_2} T(E)s(E)\,\mathrm{d}E}{\int_{E_1}^{E_2} s(E)\,\mathrm{d}E} = \frac{\int_{E_1}^{E_2} \mathrm{e}^{-\mu'(E)a}\, s(E)\,\mathrm{d}E}{\int_{E_1}^{E_2} s(E)\,\mathrm{d}E} \tag{5.11}$$

where $T(E)$ is the transmittance and $s(E)$ is the normalised spectrum of the incoming photons with $\int_0^\infty s(E) = 1$. As a consequence, the effective mass attenuation becomes:

$$\mathrm{e}^{-\mu'_{\text{eff}}a} = T_{\text{eff}} \quad \Longleftrightarrow \quad \mu'_{\text{eff}} = -\frac{1}{a}\ln T_{\text{eff}} = -\frac{1}{a}\ln\left(\frac{\int_{E_1}^{E_2} \mathrm{e}^{-\mu'(E)a}\, s(E)\,\mathrm{d}E}{\int_{E_1}^{E_2} s(E)\,\mathrm{d}E}\right). \tag{5.12}$$

In the case of more material components, an effective mass attenuation coefficient is necessary for every component except the first one. Without change to the total transmittance, the materials can be considered to be arranged in separate slices for each material and in an arbitrary order. The effective transmittance within one energy channel of the m^{th} component can be written as:

$$T_{\text{eff},m} = \frac{\int_{E_1}^{E_2} \mathrm{e}^{-\mu'_m(E)a_m}\, \mathrm{e}^{-\sum_{k=1}^{m-1}\mu_k(E)a_k} s(E)\,\mathrm{d}E}{\int_{E_1}^{E_2} \mathrm{e}^{-\sum_{k=1}^{m-1}\mu'_k(E)a_k} s(E)\,\mathrm{d}E}, \tag{5.13}$$

and thus the mass attenuation becomes:

$$\mu'_{\text{eff},m} = -\frac{1}{a_m}\ln T_{\text{eff},m}. \tag{5.14}$$

To compute these corrected attenuation coefficients for the material reconstruction, the areal densities need to be known. They are actually the result of the material reconstruction and therefore they have to be calculated iteratively. In this case, the chosen order of the materials must not be altered. Figure 5.3 shows a block diagram of an iteration cycle. It starts with initial values for the areal density vector $\mathbf{a}$ with the components $a_1, \ldots, a_k$. Regarding these, the effective attenuation coefficients can be calculated, which are the columns of the Matrix $\mathbf{M}$ with the pseudo inverse $\mathbf{M}^+$. Starting from this, an estimation for $\mathbf{a}$ can be calculated accord-

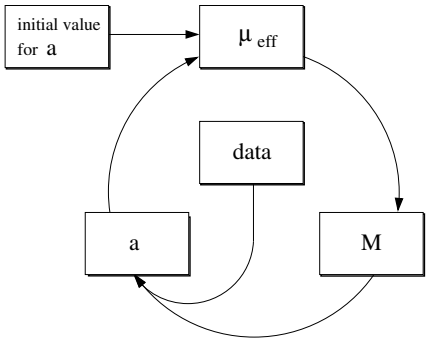

Figure 5.3 Block diagram of iterative material reconstruction.

ing to equation (5.8) and the next cycle can be started. In the practical application, it converges quite quickly and only 5–10 iterations are necessary.

This variant of material reconstruction relies on accurate spectroscopic data. Therefore it is essential to perform spectrum reconstruction beforehand, if using a detector like the Medipix2.

5.4.4 Combination Method

Another possibility is to combine spectrum reconstruction and the actual material reconstruction into one step. Spectrum reconstruction is a linear transformation on the measurement data while the material reconstruction is a transformation on the logarithmised data. Therefore they cannot be merged serially. Instead, the detector response is included in the likelihood function (see equation (5.10)).

The number of events registered in one energy channel $\tilde{N}_i$ of a pixel is then of the form $\tilde{N}_i = \sum_j R_{ij} N_j$, where R is the detector energy response as described in section 1.3 and 4.1. The part referring to the transmitted spectrum needs to be expanded, so that the energy response is taken into account:

$$N_j = N_{0,j} \mathrm{e}^{-\sum_k \mu'_{jk} a_k} \quad \Longrightarrow \quad \tilde{N}_i = \sum_j R_{ij} N_{0,j} \mathrm{e}^{-\sum_k \mu'_{jk} a_k}. \tag{5.15}$$

To account for the relatively broad energy channels used in measurements, finer channels are internally used. The L adjacent large channels meet at the energies $E_l = E_1, E_2, \ldots, E_L$. The finer channels i can be summed up to match the broader channels, so that counts in the broad channels become $\tilde{\tilde{N}}_l = \sum_{\substack{i \\ E_l \le E_i < E_{l+1}}} \tilde{N}_i$ The negative

index	maximum	description
i	N	energy deposition channel
j	J	primary photon energy channel
k	K	basis materials
l	L	energy deposition channel at measurement

Table 5.1 Overview of the indices used in section 5.

log-likelihood function $F(a_1, \ldots, a_k)$ is then:

$$F(a_1, \ldots, a_k) = \text{const.} + \sum_l \frac{\left(\tilde{\tilde{N}}_l - \sum_{\substack{i \\ E_l \le E_i < E_{l+1}}} \sum_j R_{ij} N_{0,j} \mathrm{e}^{-\sum_k \mu_{jk} a_k} \right)^2}{2N_l''} \tag{5.16}$$

The combination method offers more flexibility as it is not limited to the constraints of the spectrum reconstruction. However, computing time is about two orders of magnitude larger. Table 5.1 shows the indices used in this section to avoid confusion.

5.5 Material Reconstruction in CT

The method of material reconstruction has also been transferred to computed tomography.

The sinogram produced with a CT scan shows the projection images of the object as a diagram with respect to the projection angle and the detector element. Therefore, it represents the Radon transform of the distribution of attenuation coefficient μ of the object as shown in section 2.2. As described in the previous sections, the material reconstruction method delivers the projected densities a_k of the basis materials k of an object.

$$a_k(r, \theta) = \int \rho_k \, \mathrm{d}s \tag{5.17}$$

When compared to equation (2.2), it becomes obvious that the material reconstructed sinogram $a_k(r, \theta)$ represents the Radon transformation of the partial densities ρ_k of the basis materials. Consequently, the inverse Radon transform of the projected density $a_k(r, \theta)$ – or an implementation thereof, such as filtered back projection – leads to the partial densities of the respective basis materials k.

6 Enlarged Field of View Technique

Due to limits in processing of ASICs and bump bonding techniques, hybrid photon counting detectors like the Medipix2 can only be assembled in limited size at a reasonable price. One way to compensate for that drawback is to tile multiple chips resulting in a larger one. As the Medipix2 is three-side buttable, it is possible to form a $2 \times n$ array. A 2×2 array called Medipix2 Quad is available to the collaboration. The move and tile method [Pfe04] where the detector is moved between acquisitions and the images are combined afterwards is also possible. But this technique has some major disadvantages: It is more complex to set up, as an additional axis is required, and it is time consuming to attain the higher number of individual acquisitions. Furthermore, it introduces another source of misalignment. A third method to increase the field of view (FOV) is sinogram reflection. For fan beam geometry, it has been used since the early days of CT [NBC+79]. The FOV can be increased by up to a factor of two, when the detector is moved outward by up to half of its diameter d. The missing X-ray paths can be gained from the available data, if a full 360 degree rotation is done.

The reflected pixels can be found under the projection rotated by $180° + 2\gamma$ with γ

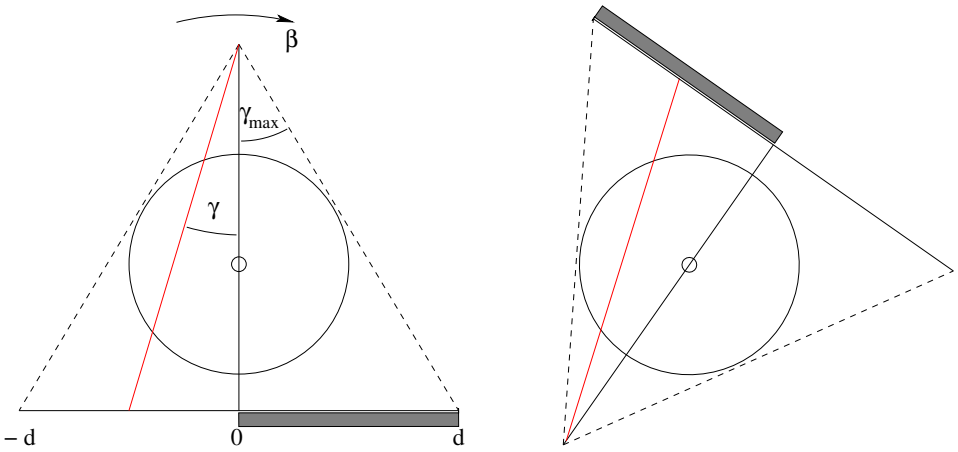

Figure 6.1 An X-ray on the side without detector cannot be detected (left image, $\beta = 0°$), the missing X-ray can be found in another projection with rotation angle $180° + 2\gamma$ (right image, $\beta = 180° + 2\gamma$)

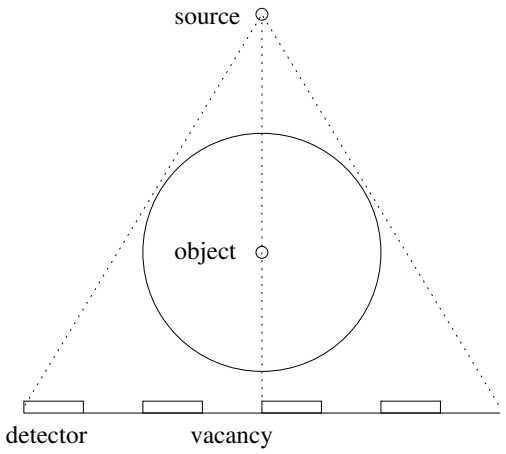

Figure 6.2 Sinogram reflection with multiple vacancies

being the angle to the center ray. On the hand left side of Fig 6.1 a setup with a detector moved to the right by $\frac{d}{2}$ is shown. For example, the ray under the angle γ, in this case 18°, does not hit the detector. On the right hand side of Fig 6.1, the rotation by $180° + 2 \cdot 18° = 216°$ can be seen. It shows the same ray path from the other side — the complementary ray — which hits the detector. Recently, this method has been enhanced for use not only in fan beam geometry, but also in cone beam geometry [ZTS05].

The asymmetric detector position can be expanded for multiple single detectors and will be presented here for fan beam geometry. The detector line is considered to be virtual and is divided into real and logic detector parts. The vacancies in the real detector arrangement are the logical parts in a periodic grid. To allow the subsequent reordering (reflection) into a non-truncated data set, at least one of two complementary rays must be detected. Thus, at a given distance from the center of the detector row, either at one or the other side, a real detector element must be present. A possible realisation can be seen in figure 6.2.

This technique allows the construction of a detector system for computed tomography using only the currently available, small detectors. It can be used to avoid the very complicated and expensive process of seamless tiling.

Part III

Measurements and Results

7 Experimental Setup

The measurements were carried out in a cabin shielded with 6 mm thick lead inside the X-ray lab. The cabin has a base area of $4.6 \times 1.8\,\mathrm{m}^2$ and can be entered through a sliding door. Inside is a table with an aluminum board on top with threaded holes on a $50 \times 50\,\mathrm{mm}^2$ grid to mount the experimental gear.

7.1 X-ray Source and Periphery

The X-ray source inside the cabin is a Siemens Megalix CAT X-ray tube, originally used in angiography, driven by a Polydoros A100 high voltage generator outside the shielded cabin. It is controlled by the CAN test-box which receives the control sequences via serial interface from a PC. A custom-designed software called "polydoros" running on this PC creates the control sequences according to the user input and sends it to the test-box. The technical specifications of the X-ray source can be found in table 7.1.

The Medipix2 detector is controlled by the Pixelman software [PJH, HJP+06], developed by the IEAP, CTU Prague. It is connected to a PC using either the USB read-out [Vyk05] or the MUROS2 [BvBJ+03] combined with a National Instruments DIO-32HS card.

property	value
acceleration voltage	40–125 kV
current	1–800 mA
maximum continuous power	2500 W
focal spot size	large: 1 mm, small: 0.6 mm, micro: 0.3 mm
anode material	tungsten-rhenium

Table 7.1 Properties of the Megalix CAT125 with the Polydoros A100 X-ray source according to the data sheet provided by the manufacturer.

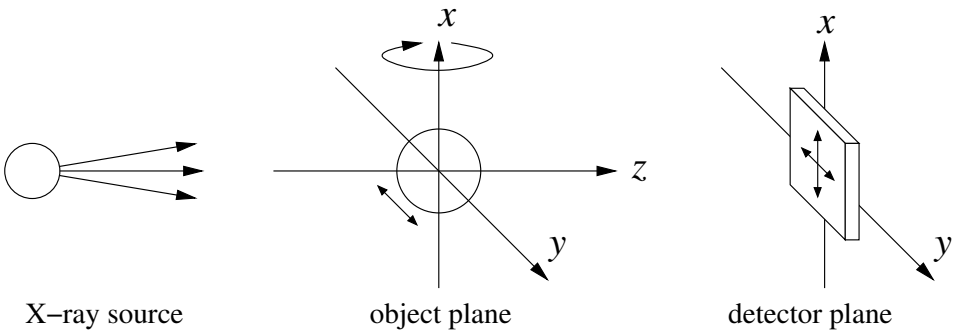

Figure 7.1 Schematic of the X-ray lab setup with source, object and detector plane including the axis denominations. The detector can be moved along the x- and y-axis and the object along the y-axis. For tomographic scans, the object can also be rotated around the x-axis.

7.2 Imaging Setup

Due to the small pixel size of 55 µm in the Medipix2, a precise positioning of both detector and object is necessary. To achieve this, a precise positioning system is needed. In this case, the Newport MotionControl MM4006 was used. Three translation stages to move object and detector are mounted on a table inside the shielded cabin. Figure 7.1 shows a schematic of the setup. The Medipix2 detector is mounted on two orthogonal translation axes (x and y), so it can be moved on a plane perpendicular to the beam direction (z-axis). One translation stage is used to move the object along the y-axis. Additionally there is also a rotation stage for the object to perform tomographic scans in the y-z-plane, which rotates around the x-axis. This rotation stage is mounted on two perpendicular pivot units to allow a precise adjustment of the rotation axis for the tomographic setup. The precision of the positioning stages can be found in table 7.2.

tpye of unit	precision
translation stage M-ILS CC series	2 µm
rotation stage PR50 CC series	0.1°
pivot unit with micrometer adjustment screw	0.005°

Table 7.2 Precision of the utilised positioning stages

7.3 Monochromator Setup

For detector characterisation, monochromatic radiation is needed and a simple monochromator was set up inside the cabin using the above mentioned X-ray tube as a source. As crystal, a 100 mm silicon wafer is used to get a Bragg reflection at the Si(1,1,1) surface with a lattice spacing of $d = 3.135 \cdot 10^{-10}\,\mathrm{m} = 3.135\,\text{Å}$. Constructive interference of the n-th order occurs, if Bragg's law is met:

$$2d \sin\theta = n\lambda = n \cdot \frac{hc}{E} \tag{7.1}$$

where θ is the angle of incidence, λ the wave length and E the photon energy.

Figure 7.2 shows a schematic of the setup and in figure 7.3 a photograph of the setup in the lab is shown. Since the applied energies are between approx. 20 keV and 60 keV, only small angles θ between approx. 5.7° and 1.9° appear. The distance FC (focus–crystal) is 670 mm, CD (crystal–detector) is 595 mm and the part of the crystal in the beam s is 60 mm. For angles so small that $\cos\theta \approx 1$ is a good approximation, α can be approximated with

$$\alpha \approx \arctan\left(\frac{s \sin\theta}{FC}\right). \tag{7.2}$$

In the detector plane, the angle θ correspondes to a distance in y-direction:

$$y = CD \cdot \tan(2\theta) \tag{7.3}$$

where $\theta = \arcsin\left(\frac{hc}{2dE}\right)$ according to equation 7.1 for the first harmonic. Thus, for small angles θ, y can be approximated with

$$y \approx CD \cdot \frac{hc}{Ed} \quad \text{and} \quad \frac{\mathrm{d}y}{\mathrm{d}E} \approx -CD \cdot \frac{hc}{d} \cdot \frac{1}{E^2} \tag{7.4}$$

This way, the resulting spread of monochrome radiation ("rainbow" or "fan") inpinging at the detector can be calculated.

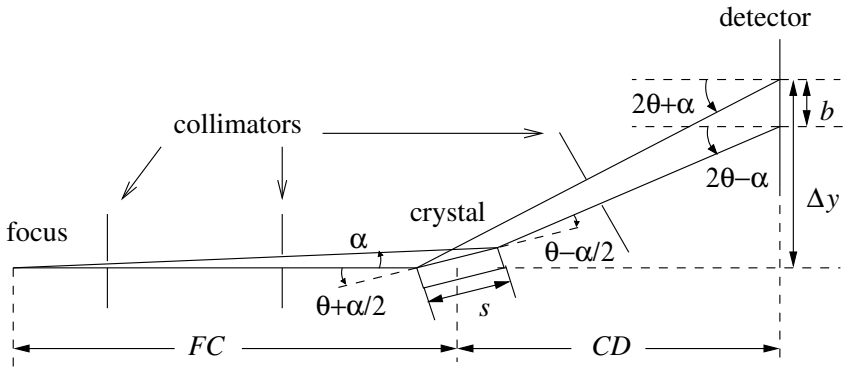

Figure 7.2 Schematic of the monochromator setup in the y-z-plane

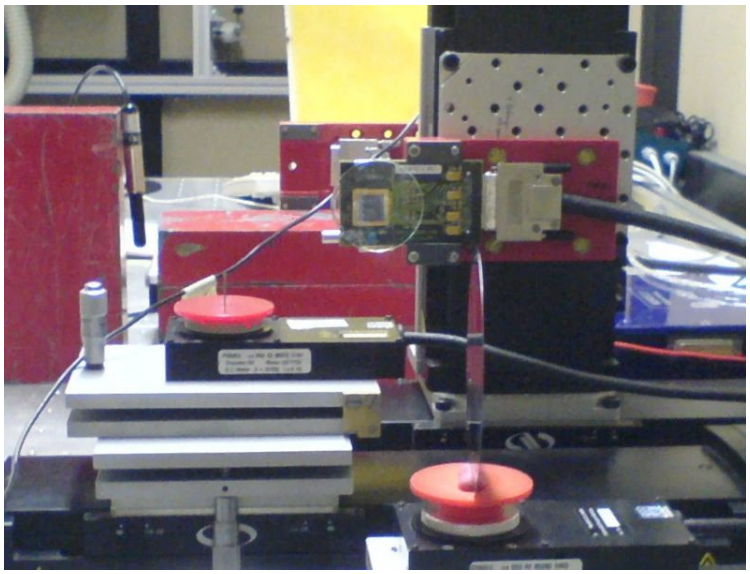

Figure 7.3 Picture of the monochromator setup without the collimators as seen from the source. In the foregound, the Si wafer can be seen with the Medipix2 detector behind.

8 Enlarged Field of View Technique

In chapter 6, a method for enlarging the field of view in a CT scan by extending the known technique of sinogram reflection was presented. Monte-Carlo simulations and measurements with the Medipix2 detector were carried out.

8.1 Monte-Carlo Simulations

At first, a phantom was implemented into the simulation. The main body of the phantom is a cylinder of water. Inside this, there are four smaller cylinders. These inner cylinders contain vacuum, air, 0.4% Gadolinium in aqueous solution and 0.4% Iodine in aqueous solution. Figure 8.1 shows the structure of the phantom in cross section. The diameter of the outer water cylinder is 200 mm, the diameter of the inner cylinders is 50 mm each.

Four detector positions with 32 elements (pixels) each and four vacancies with the same spacing were employed as shown in figure 6.2 on page 50. Since this was a simulation, both detector and its alignment were ideal. The incident X-ray energies were distributed according to a 120 kV tungsten spectrum with 0.6 mm titanium filtering. A full 360° scan with 1° steps was performed in the simulation. The number of incident photons was $5 \cdot 10^6$ per projection, so a total number of $1.8 \cdot 10^9$ photons were simulated.

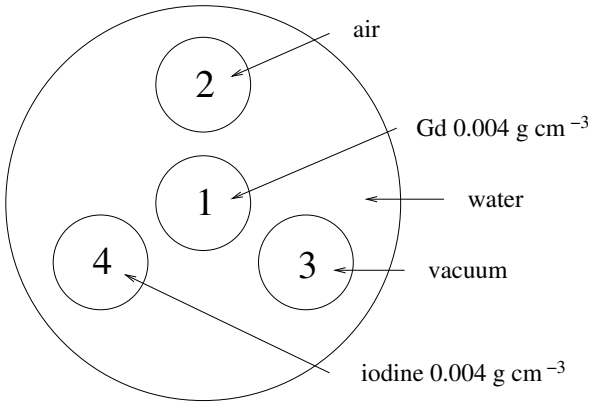

Figure 8.1 Structure of the phantom in cross section.

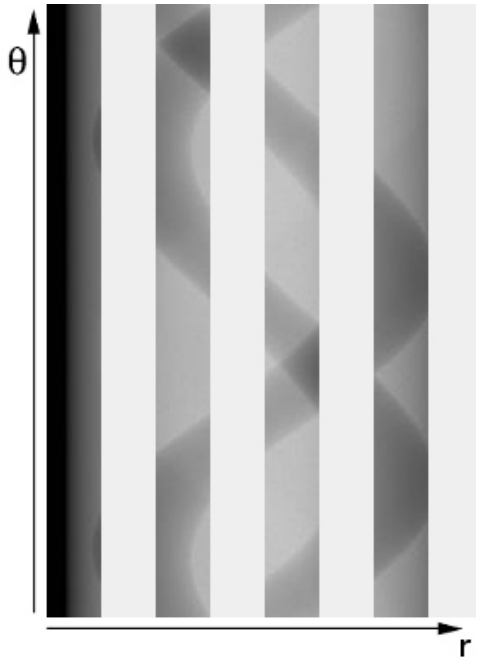

(a) The sinogram of the simulation. The empty stripes at positions without detectors are clearly visible.

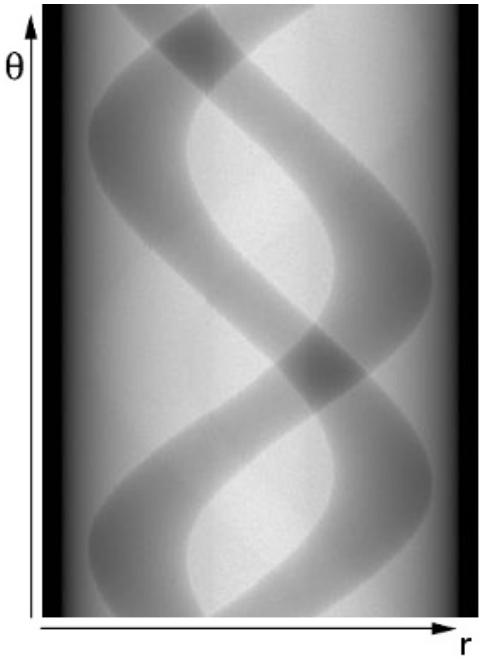

(b) The same data set after application of extended sinogram reflection.

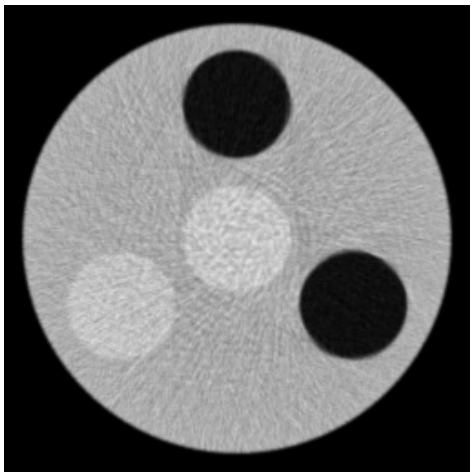

(c) Reconstructed CT slice from sinogram in (b)

Figure 8.2 Comparison of the sinograms (a) before and (b) after extended sinogram reflection and (c) the resulting CT slice.

Represented as a sinogram, the resulting data set can be seen in figure 8.2(a). The empty stripes without information due to the vacant detector positions are clearly visible. Applying the extended sinogram reflection leads to the sinogram shown in figure 8.2(b). The empty spaces are now filled with the respective complementary rays. It results in a complete sinogram, from which an CT slice can be reconstructed with a standard technique, e.g. filtered back projection. The resulting CT slice image (figure 8.2(c)) looks as expected.

8.2 Measurements

To verify the method, measurements were carried out with the computed tomography setup described in section 7.2 of the previous chapter. The analysed phantom here was a PMMA rod with 5 cm diameter with three holes (1 cm of diameter) filled with air and different concentrations of iodine solution (1% and 5% by mass). The X-ray tube was operated at 40 kV and the images were acquired with 40 mAs per projection. Overall 360 projection images over 360° were taken with a Medipix2 detector, equipped with a 300 µm silicon sensor layer at 150 V bias. Only the center row of the detector (256 pixels width) was used to maintain fan beam geometry.

The detector as a whole is virtual and consists of two real and two virtual parts. and is divided in four parts of equal size. Images were taken with the real detector elements at two of these positions (1 and 3, see 8.3(a)). The other two positions were filled applying the method of extended sinogram reflection described in chapter 6, so that the effective field of view was quadrupled.

The sinogram shown in figure 8.3(a) has vacant regions due to the missing detector positions; in figure 8.3(b), they have been filled by sinogram reflection. The pixels in this representation of the sinograms are square with the dimension 1024×360 pixels. Figure 8.3(c) shows the corresponding CT slice, reconstructed on a 512×512 pixel matrix with a $\big[\mathrm{abs}(k) \cdot \cos(k)\big]$-filter kernel. The visible ring artifact is presumably due to limited flat field correction and possible misalignment of the detector. As the simulations with ideal alignment and ideal detector response have shown, this artefact does not result from the sinogram reflection.

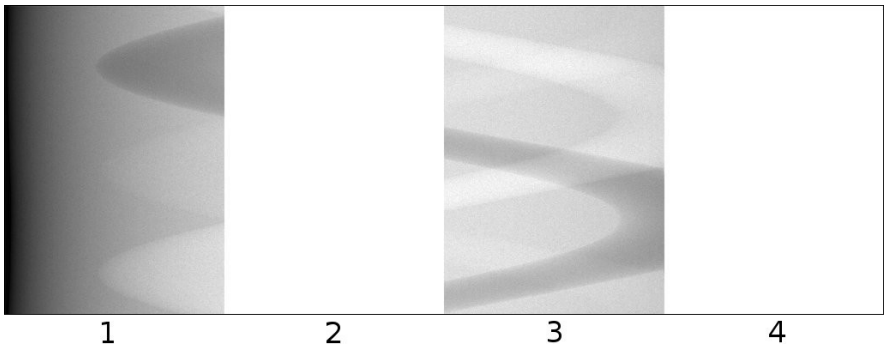

(a) The sinogram of the measurement of the phantom composed of the detector positions 1–4. The vacancies at the positions 2 and 4 are clearly visible.

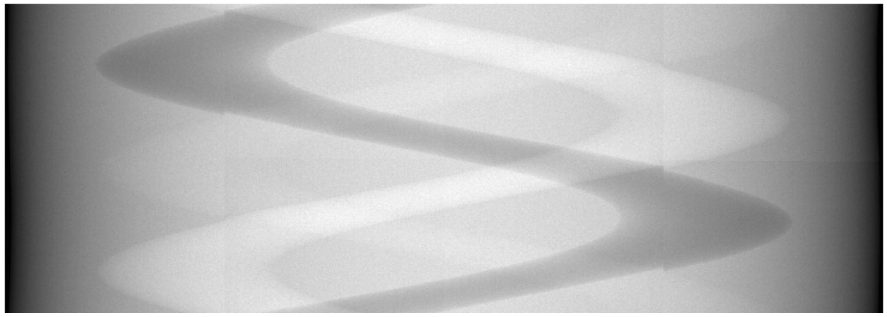

(b) The same data set after application of extended sinogram reflection. All positions are filled and a standard CT-reconstruction can be applied.

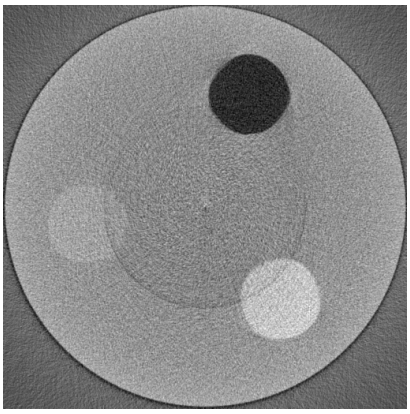

(c) Reconstructed CT slice from sinogram in (b).

Figure 8.3 Comparison of the sinograms (a) before and (b) after extended sinogram reflection and (c) the resulting CT slice.

8.3 Conclusion

A method to enlarge the field of view in fan beam geometry CT has been applied in measurements and simulations. Basing on the sinogram reflection technique it allows to use multiple small detectors to reach the desired field of view size.

Measurements have shown that the method works, but shows some artefact. Application to simulated data where absolute alignment is provided, shows that the method works properly but also indicates that the method depends on accurate alignment and detector calibration.

9 Detector Response to Monochrome Radiation

The energy response of the detector is not ideal, i.e. it delivers a distorted spectrum. This characteristic energy response is due to the effects of back-scattering, fluorescences and charge sharing. Charge sharing is an effect that distributes the charge carriers generated in the sensor layer among multiple pixels, which can lead to multiple counts originating from a single impinging photon and therefore to a shift of the energy response towards lower energies and increased count rates at low thresholds. Therefore, a deeper understanding of the energy response of the detector is necessary in order to make quantitative energy resolving measurements.

In this chapter, both measurements and Monte Carlo simulations are presented. The measurements with monochromatic radiation were also used to verify the simulation model. These results are needed later for the spectrum reconstruction and material reconstruction techniques in the subsequent chapters.

9.1 Monochromatic Measurements

As mentioned in section 1.3, a detector like the Medipix2 has a complex energy response. To understand and to model the energy response of the detector, it is necessary to know the detector response to monochromatic irradiation. A simple monochromator was set up as described in section 7.3 to allow these measurements without access to bright and monochromatic light source as available at a synchrotron.

Fig 9.1 shows an image of the tungsten $K\alpha_1$ and $K\alpha_2$-line in reflection of the employed X-ray tube at 57.98 and 59.32 keV respectively, measured at an energy threshold of 19.1 keV. Only between column 95 and 155, reflected radiation from the monochromator can geometrically reach the sensor. Thus, everything outside this region is scattered radiation. The projection along the columns is shown in figure 9.2 for the columns 80 to 160. The width of the lines is mainly due to the size of the focal spot of the source. The separation of energy is good enough to separate the Kα_1 and Kα_2 lines clearly.

A series of these measurements were acquired with increasing energy thresholds with an increment of 0.59 keV resulting in what is known as threshold scan. Selected images with different energy thresholds can be seen in figure 9.3. Due to charge

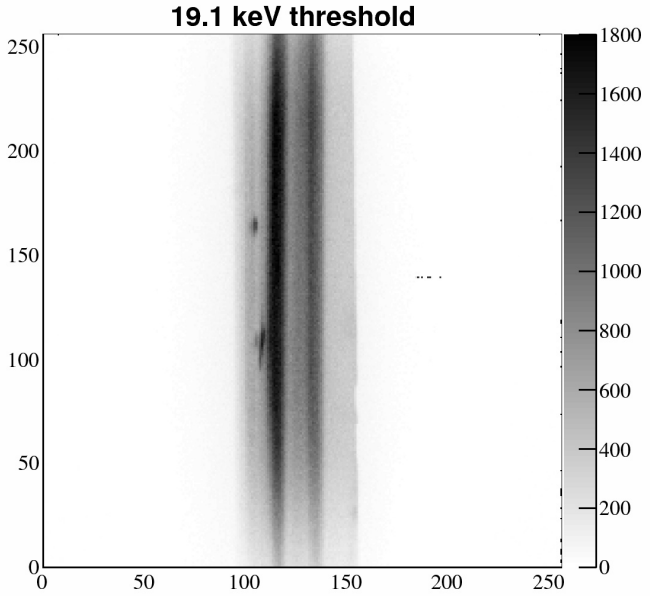

Figure 9.1 256 by 256 pixel picture of tungsten Kα lines taken with the Medipix2 at an energy threshold of 19.1 keV. The diffraction angle decreases from left to right, i. e. the photon energy increases. The left line is the Kα_1 and the right line is the less intense Kα_2.

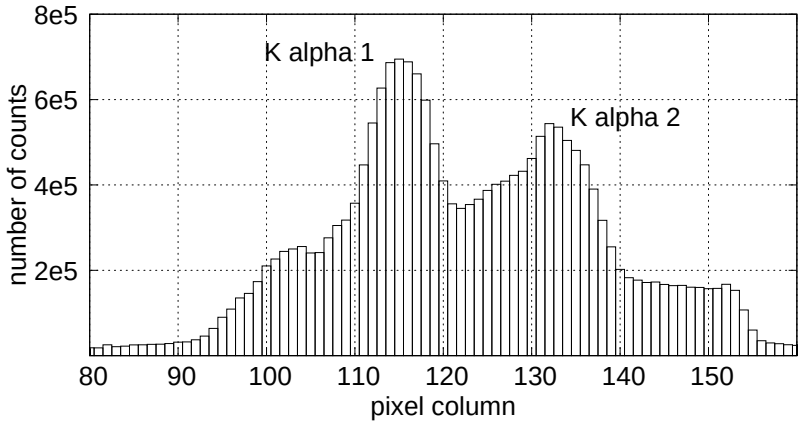

Figure 9.2 Projection of tungsten Kα lines from fig. 9.1. The energy difference of 1.34 keV between the Kα_1 and the Kα_2 line can be differentiated clearly.

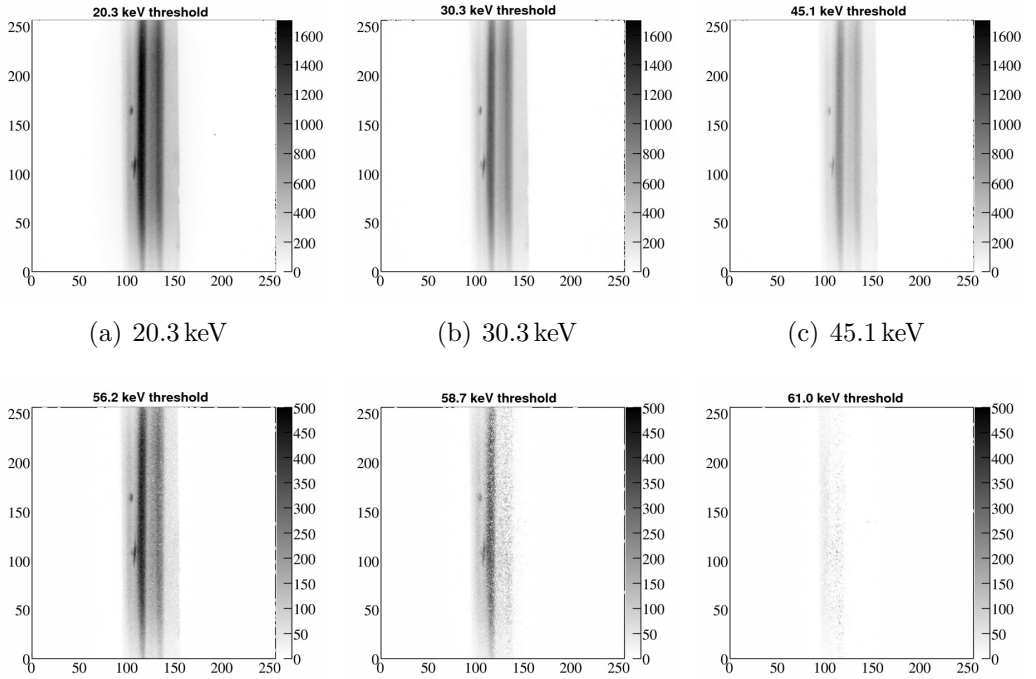

(a) 20.3 keV (b) 30.3 keV (c) 45.1 keV

(d) 56.2 keV (e) 58.7 keV (f) 61 keV

Figure 9.3 The Kα-lines of tungsten at different thresholds. With increasing threshold, the number of counted photons decreases and becomes zero with the threshold energy reaching the photon energy.

sharing, the number of counted photons decreases with increasing threshold, even for monoenergetic impinging photons. At energy thresholds above the primary photon energy, the count rate is zero. However, the global threshold shows pixel-to-pixel variations and some pixels may still count events. The images shown in figure 9.3(d)-(f) were taken with threshold energies close to the Kα fluorescence energies. At 56.2 keV (figure 9.3(d)), below both the Kα_1 at 59.3 keV and the Kα_2 line at 58.0 keV, both lines are visible. In figure 9.3(e), at an energy threshold just between the two lines, only the Kα_1 can still be seen. As expected, with the threshold above the energy of the Kα_1, neither of the lines can be observed (figure 9.3(f)), except some "noisy" pixels.

The difference of the detected photons between adjacent energy thresholds results in the number of photons in the respective energy channel. Together, these channels form the detector system's energy response spectrum at the impinging photon energy.

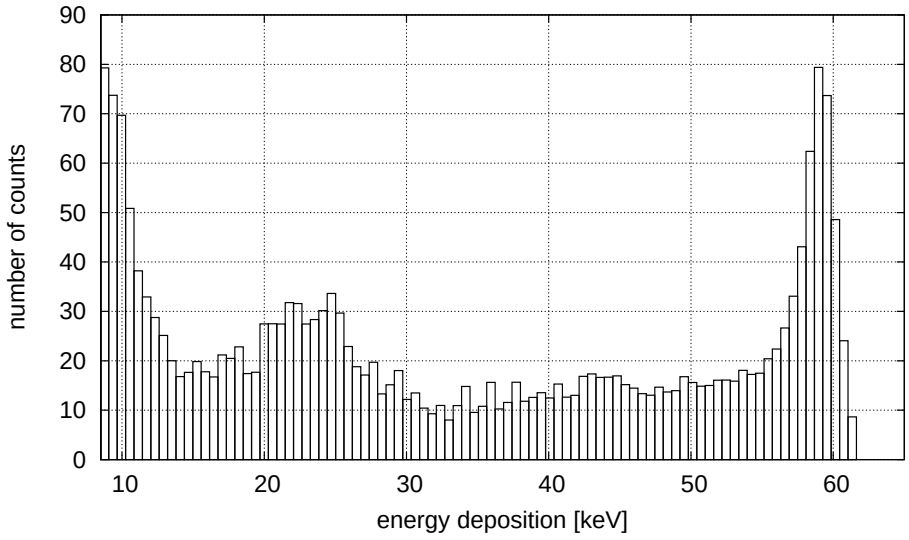

Figure 9.4 Measurement of the energy response of the Medipix2 to 59.3 keV incident photons. Noticable the Compton edge at 11 keV and the photo peak at the primaty energy. The weaker peaks at 22 keV and 25 keV are silver and tin fluorescenses.

This method is called differentiated threshold scan.

The energy response of the Medipix2 with a 300 µm silicon sensor layer acquired by this means can be found in figure 9.4. To increase the photon statistics, the mean value over all pixels of columns 112 through 119 is shown. The dominant peak at the primary energy is due to the photo electric effect, where the entire photon energy (less the binding energy of the electron) is transferred to a single electron in the sensor. This peak is usually referred to as the photo peak. The plateau below that energy is due to charge sharing between pixels, i. e. some of the generated charge reaches into the neighboring pixel and is therefore missing in the primary pixel. Tin is present in the bump bonds used to connect the sensor layer to the ASIC and silver in the glue used to connect the ASIC to the PCB. As a result of the presence of these elements, their fluorescence peaks (silver at 22 and tin at 25 keV) are also visible. The steep slope at 11 keV is the Compton edge, corresponding to the primary photon energy of 59.3 keV (compare equation (1.1) on page 20).

As this energy response shows a complex structure, it cannot be easily analytically calculated. Instead, Monte Carlo simulations were done; these are described in the following section.

9.2 Monte Carlo Simulations and Comparison to the Measurement

One possibility to model the energy response of a pixelated detector is to get the mean energy deposition distribution with respect to the energy from a Monte Carlo simulation and convolve it with the pixel aperture [NDHB02, Tlu05]. These methods only work well for high photon statistics but show limitations when working with single events. Therefore the physical model of charge sharing between pixels and charge carrier propagation have been fully implemented in the Monte-Carlo simulation.

The Monte-Carlo simulations presented here are carried out using the simulation tool ROSI. It was extended to take into account charge sharing, propagation of the charge carriers in the sensor layer and back scattering as described in section 3.3. The simulation is compared with measurements averaged over several hundred pixels. Therefore the pixel-to-pixel variations and electronic noise are included in the total noise. For the simulations presented here, a total noise of 190 electrons rms is assumed, that corresponds to 0.684 keV when using a silicon sensor.

Figure 9.5 and figure 9.6 show the simulation and the measurement of the energy response to incident photons with an energy of 33.2 keV and 59.3 keV respectively. The Monte Carlo simulation can reproduce all of the structures mentioned in chapter 1.3 in the energy response spectrum of the Medipix detector. At 190 electrons overall noise for pixel to pixel and electronic noise, the photo peak shows the same peak width and peak-to-valley characteristics, i.e. the ratio between peak height and plateau is the same. As the concentration of silver and the thickness of the layer of the silver containing glue can vary and is not known exactly, it was varied in the simulation to match the measurement. For the Medipix2 detector assembly used for these measurements, best agreement was achieved with a thickness of 14 µm for the silver layer. The Compton edge seen in figure 9.6 also shows the correct position and slope.

Figure 9.7 shows a chart of the energy response against the primary photon energy. A single line of that chart corresponds to a diagram as in figure 9.5 or 9.6. The primary energies were simulated in steps of 0.5 keV with 0.1 keV binning in the energy deposition domain. Each primary energy was simulated with 10^7 incident photons. The diagonal line, where the energy deposition is close to the primary energy, is due to the photo effect. Even on a logarithmic scale, the strong decrease of the cross section of the photo electric effect is evident. Together with the increasing effect of charge sharing with higher energies, this leads to disappearance of the photo peak in favor of a large plateau for primary energies above 100 keV. Also very good

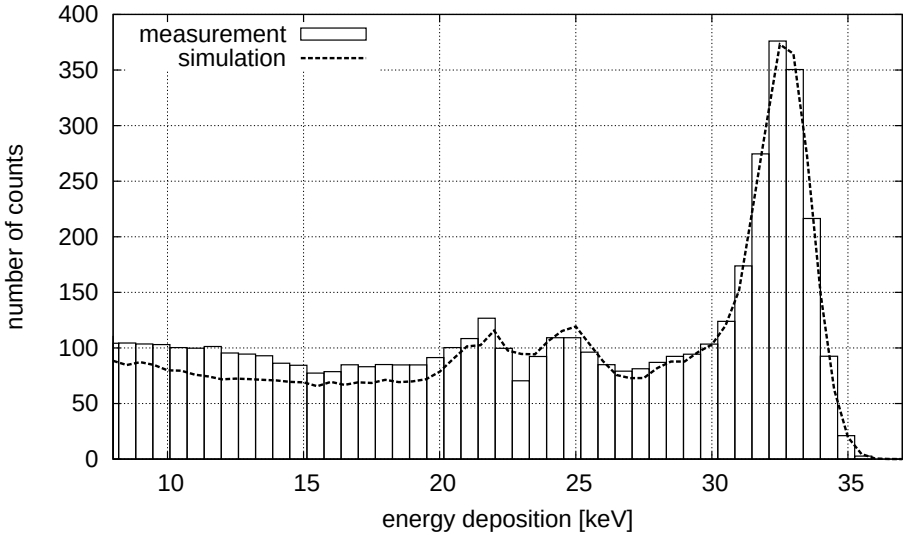

Figure 9.5 Comparison of measurement and simulation of the energy response of the Medipix2 to 33.2 keV incident photons. The simulation and measurement match very well. The higher number of events below 20 keV are due to scattered radiation.

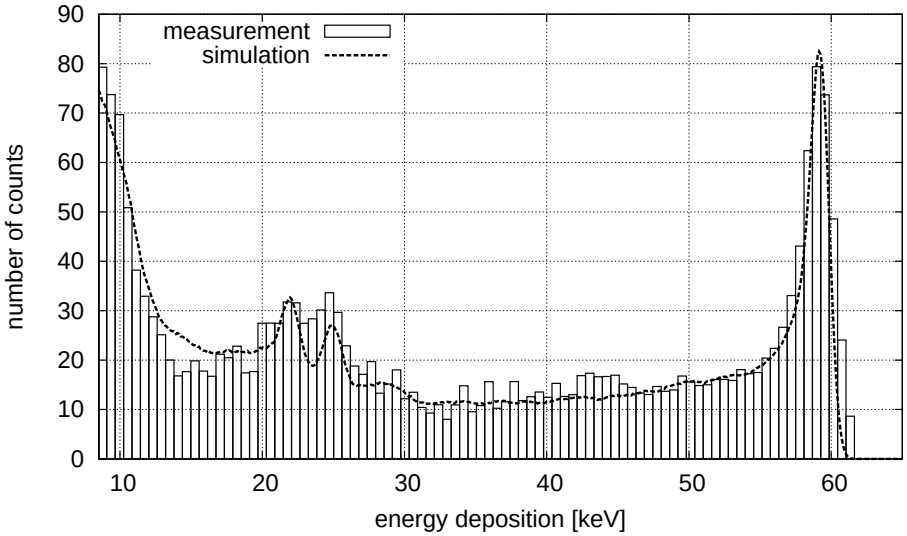

Figure 9.6 Comparison of measurement and simulation of the energy response of the Medipix2 to 59.3 keV incident photons.

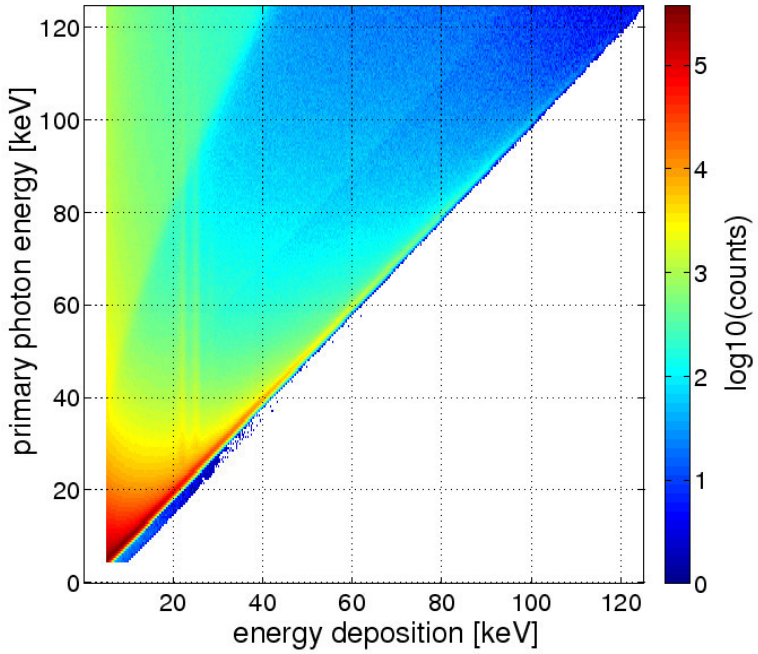

Figure 9.7 Chart of the energy deposition against the primariy photon energy.

visible is the Compton edge. It can be observed from a primary photon energy of approximately 50 keV, where the maximum energy transfer is 8.2 keV according to equation (1.1). It progresses to 41 keV at a primary energy of 125 keV. Remarkable are also the fluorescence lines of silver and tin at 22 and 25 keV as they remain at fixed energies and appear as vertical lines in this chart.

9.3 Conclusion

In this chapter, the detector energy response of the Medipix2 detector to monochrome radiation was investigated. The complete detector assembly of the detector has been included in a Monte Carlo simulation to take backscattering and fluorescese radiation into account. Furthermore, a physical model of charge sharing has been implemented in the simulation. Measurements and Monte Carlo simulations were accomplished and compared.

The good agreement between simulation and measurement indicates that the effects influencing the energy response of the detector are well understood and have been successfully modeled into a Monte Carlo simulation. A complete set of energy response functions has been simulated for the energy range from 5 keV to 125 keV.

10 Spectrum Reconstruction

As described in the previous chapter, the energy response of a pixelated semiconductor X-ray detector is far from ideal. But the knowledge of the spectral response functions to monoenergetic irradiation allows to correct for it and hence gain the original incoming spectrum. The method exploits the knowledge of the detector response to monoenergetic irradiation obtained from Monte Carlo simulations presented in the previous chapter. The two implementations of the method introduced in chapter 4 are applied and the results are presented.

The spectrum reconstruction is a key method for the material reconstruction. Spectrum reconstruction allows the access to the real spectrum impinging on the detector rather than the energy deposition in the sensor layer. Only the knowledge of the spectrum provides the possibility of a quantitative reconstruction of the material components since it depends on the attenuation coefficient of the respective material, which itself is a function of photon energy.

10.1 Complete Detector

The Siemens Megalix CAT 125 with tungsten anode as introduced in chapter 7 has been used as X-ray source. The data was acquired through a threshold scan of the lower threshold and averaging over all pixels of the detector. The energy threshold ranged from just above the noise limit of the detector (approximately 6 keV) to well above the maximum energy, i. e. the corresponding acceleration voltage.

10.1.1 Matrix Inversion Method

Figure 10.1 and 10.2 show the reconstructed spectra from the X-ray tube compared to the expected one for 50 and 120 kV acceleration voltage. The expected spectra were generated according to Boone's model [BS97] and scaled to the same integral value as the one reconstructed from the measurement. This normalisation is necessary since the photon flux from the source is not known exactly. In all three cases, the reconstructed spectra are in good agreement with the expected ones. Both the increasing and the decreasing slope of the spectrum is matched very well as well as the characteristic K-lines visible at 59 keV in the 120 kV spectra.

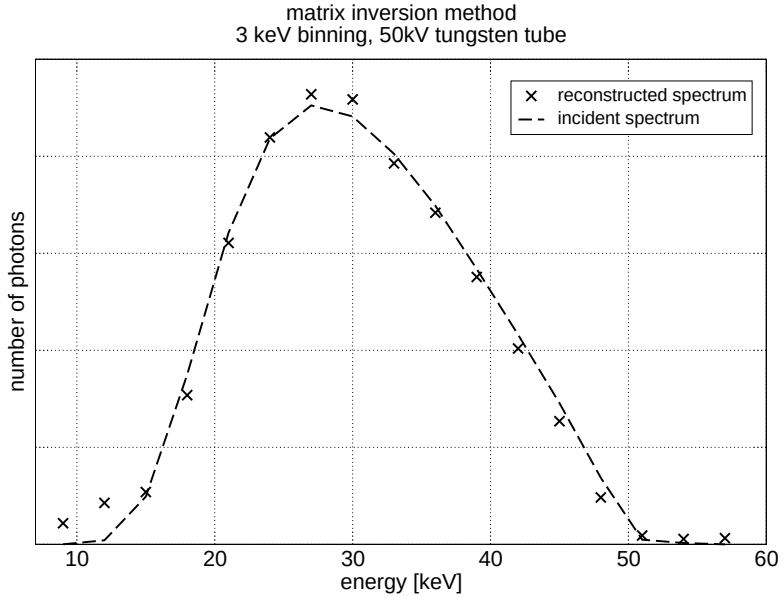

Figure 10.1 Reconstructed 50 kV tungsten spectrum using matrix inversion.

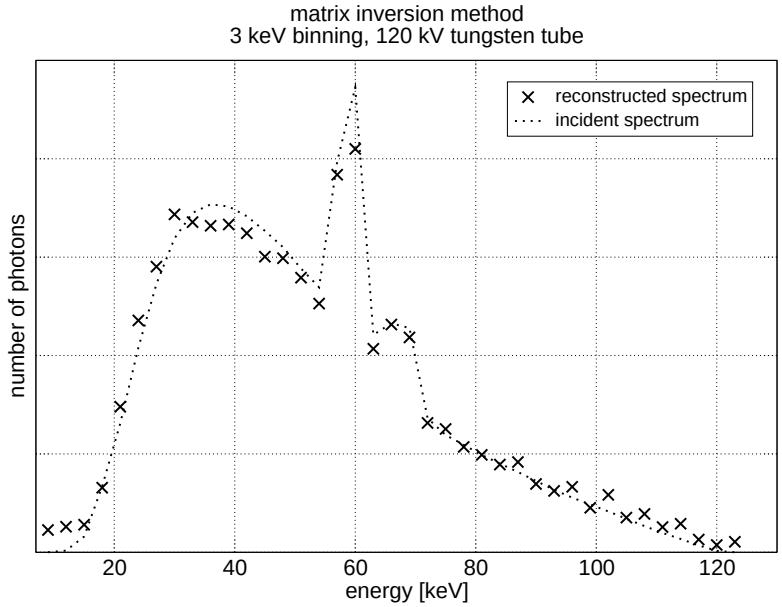

Figure 10.2 Reconstructed 120 kV tungsten spectrum using matrix inversion.

The reconstruction of the 120 kV spectrum shows an increased noise at energies above 80 keV. This is presumably caused by two different reasons. On one hand, the decreased photon statistics are due to the decreasing detection efficiency of the 300 µm silicon sensor layer at the higher energies which lead to a higher noise. On the other hand, the response functions of adjacent energy channels lose their significance as the photo peak vanishes and the Compton edge changes more slowly with energy (see figure 9.7).

At energies of 12 keV and below, the reconstructed spectra are clearly higher than expected. As this applies to both spectra, it appears to be a systematic error. One reason would be the slight underestimation of the energy deposition at lower energies as can be seen in figure 9.5 or the presence of lower energy scattered radiation and lead's L-fluorescensce in the measurements.

10.1.2 Spectrum Stripping

Spectrum stripping also works very well for spectrum reconstruction. The reconstructed spectra are very close to the expected spectra, as can be seen in figure 10.3 and 10.4. Overall, spectrum stripping shows very similar results to matrix inversion. At an energy bin size of 3 keV and with less than 40 energy bins in the reconstructed spectrum, the differences are invisible to the naked eye. This includes the10^{10} photons $s^{-1}cm^{-2}$ too high and presumably false reconstructed values at energies below 15 keV. This indicates a systematic error either in the simulated response functions or a difference of the real spectrum to the expected one. Two possible reasons for differing from expected spectrum are scattered radiation and L-fluorescense of lead inside the shielded cabin.

10.1.3 Comparison between Matrix Inversion and Stripping

As seen in the previous section, both methods of spectrum reconstruction show very similar results while using relatively few and wide energy bins. However, when using smaller energy bins for the spectrum reconstruction, the stripping method has an advantage over the matrix inversion method. This can be seen in figure 10.5 which shows the reconstructed 70 kV tungsten spectrum reconstructed with both matrix inversion and spectrum stripping. With 1 keV energy bin size and an overall number of 68 bins, the spectrum reconstructed with the matrix inversion method shows much higher noise. With decreasing energy bin size, the matrix inversion method completely fails due to numerical reasons, i. e. the difference between the energy response functions becomes so small that they cannot be treated as linearly independent and the matrix inversion fails numerically. With a maximum energy of

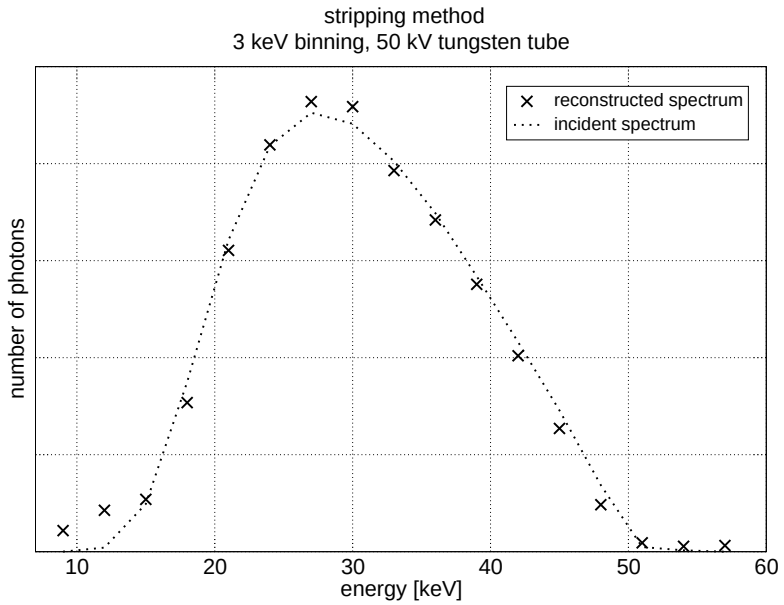

Figure 10.3 Reconstructed 50 kV tungsten anode X-ray spectrum using spectrum stripping.

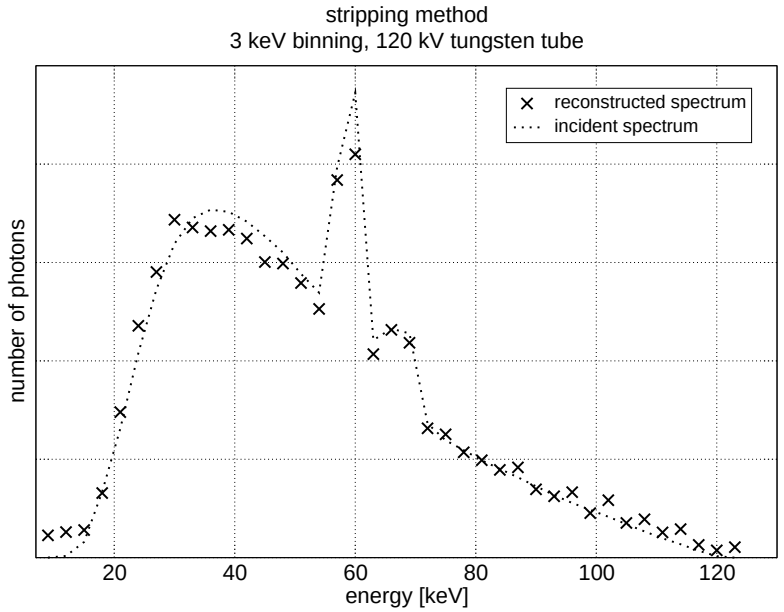

Figure 10.4 Reconstructed 120 kV tungsten anode X-ray spectrum using spectrum stripping.

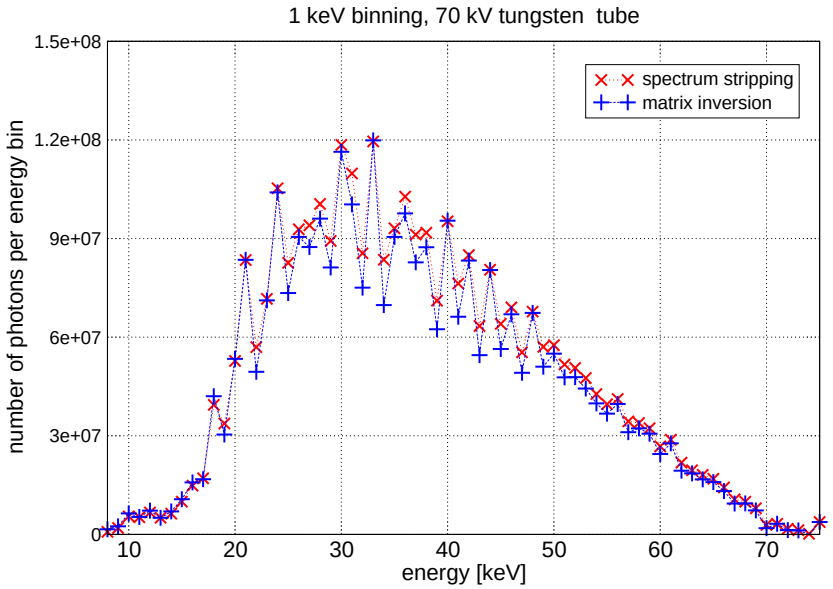

Figure 10.5 Comparison between stripping and matrix inversion with 1 keV binning. The spectrum reconstructed by the matrix inversion method shows higher noise than spectrum stripping. Since both are reconstructed from the same data set, the noise is correlated.

70 keV, this is the case with energy bins smaller than 1 keV or around 1.5 keV for energies up to 120 keV. The spectrum stripping method still yields results, albeit increasingly noisy.

In order to allow a quantitative comparison, the squared deviation σ^2 from the expected spectrum was calculated:

$$\sigma^2 = \sum_i (N^{\text{in}} \cdot s_i - N_i^{\text{reco}})^2 \tag{10.1}$$

where N^{in} is the total number of impinging photons, s_i the expected spectrum normalised to one photon and N_i^{reco} the reconstructed number of photons. Since the absolute photon flux from the source is not known, N^{in} was obtained by minimising the root of the squared deviation σ. Table 10.1 shows the deviation of the reconstructed spectra from the expected ones for a 70 kV tungsten spectrum for different energy bin sizes and the two different reconstruction methods. For 2 and 3 keV bin sizes spectrum stripping shows only a slightly smaller σ, but for 1 keV bin size, matrix inversion results in a considerably higher deviation. As the spectrum stripping method is at least as good as the matrix inversion method and often better, it will

method	spectrum range	binning	N^{in}	σ
stripping	15–72 keV	3 keV	$2.98 \cdot 10^9$	$5.063 \cdot 10^7$
matrix inversion	15–72 keV	3 keV	$2.97 \cdot 10^9$	$5.071 \cdot 10^7$
stripping	15–73 keV	2 keV	$3.02 \cdot 10^9$	$4.439 \cdot 10^7$
matrix inversion	15–73 keV	2 keV	$2.99 \cdot 10^9$	$4.523 \cdot 10^7$
stripping	15–72 keV	1 keV	$3.18 \cdot 10^9$	$6.466 \cdot 10^7$
matrix inversion	15–72 keV	1 keV	$3.00 \cdot 10^9$	$8.104 \cdot 10^7$

Table 10.1 Comparison between matrix inversion and spectrum stripping spectra reconstruction for a 70 kV tungsten spectrum. N^{in} and σ are absolute values and represent the number of photons.

be used exclusively for the rest of this work.

10.2 Single Pixel

The spectrum reconstruction was also applied to single pixels. Figure 10.6 shows the reconstructed spectra of a 40 kV tungsten spectrum of three different pixels. The number of impinging photons per pixel is approximately 18,000, and due to the relatively poor detection efficiency originating from the 300 µm silicon sensor layer, the number of counted events is approximately 4,000 at a threshold of 5 keV. However, it decreases to a few tens of counts at thresholds above 35 keV. These decreased photon statistics lead to increased noise, especially at the higher energy part.

The insufficient statistics can be countered with higher photon flux or by summation over several pixels. The nine-fold statistics of a 3×3 pixel cluster with approximately 170,000 photons lead to a much smoother reconstruction which can be seen in figure 10.7.

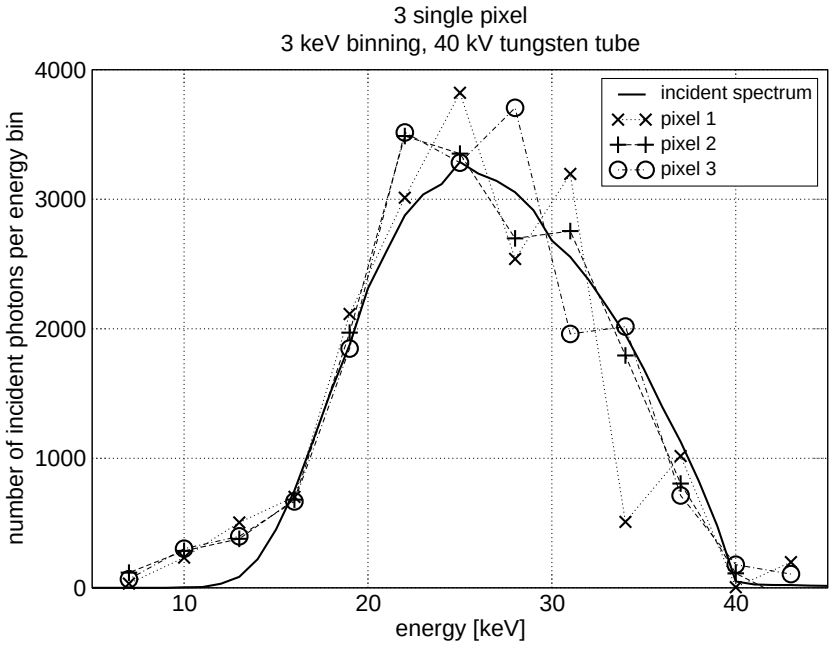

Figure 10.6 Examples of pixel-wise spectrum reconstruction

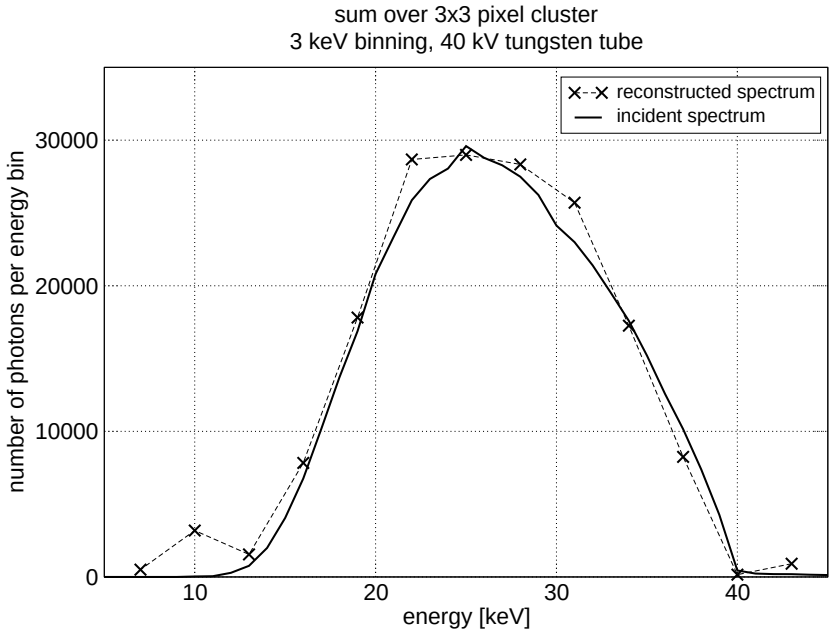

Figure 10.7 Spectrum reconstruction of a 3x3 cluster

10.3 Conclusion

It has been shown in this chapter that the reonstruction of the incident spectrum is possible, provided the detector energy response to monochromatic radiation is known.

Two implemetations of the method (spectrum stripping and matrix inversion) have been applied to Medipix2 measurements at a series of energy thresholds. The incident X-ray spectra have been reconstructed successfully. Spectrum stripping proved to be more stable and accurate, especially when using a fine energy sampling. The method can also be applied to single pixels, provided a sufficient photon statistic is available.

Unlike other spectrometers, the spectrum reconstruction technique in combination with the Medipix2 detector allows to measure an X-ray spectrum even at high flux up to a count rate of 10^{10} photons $s^{-1}cm^{-2}$ and offers additional spatial resolution.

11 Material Reconstruction

Material reconstruction is a material decomposition technique. In contrast to other material decomposition techniques like the dual energy approach, it provides the areal densities of a given set of basis materials and is not limited to two material components. Instead of employing different source spectra, material reconstruction relies on the energy information obtained from a spectroscopic detector.

The method can be used in both radiography and computed tomography. In radiography it delivers the areal densities of applied basis materials, while in CT it directly provides their partial volumetric densities. The combination of the respective densities leads to the same total attenuation as the composed object.

The different versions of material reconstruction technique introduced in chapter 5 are applied to radiography and computed tomography situations, both in simulation and measurement.

11.1 Material Reconstruction in Radiography

11.1.1 The Phantom Setup

A phantom was set up to investigate the capabilities of the method in a radiography situation. The phantom consists of a PMMA[1] cube with 3 cm side length and a cutout of $1 \times 2 \times 2.5\,\mathrm{cm}^3$ which is filled with a 1.2% iodine dilution resulting in a concentration of 13.5 mg iodine per cm^3. Furthermore, a 2 mm thick aluminum sheet was placed over the lower left corner of the imaged frame.

Figure 11.1 shows a sketch of the setup from two different views. In figure 11.1(a) a view from top, i. e. onto the x-z-plane of the setup is shown. In figure 11.1(b) the resulting image as seen on the detector is outlined and the different regions are marked. Region 0 is just the open beam. Regions 1 and 3 are covered by 2 mm aluminum, while region 3 has an additional 30 mm PMMA coverage. Region 2 and 4 are covered by PMMA only, 30 mm in region 2 and 10 mm in region 4. Region 5 has a coverage of 10 mm PMMA and 20 mm water with 1.2% iodine solved. An overview of the coverage of the different regions can be found in table 11.1. Figure 11.2(a)

[1] Poly(methyl methacrylate). It is commonly called acrylic glass and also known under trade names like Plexiglas, Perspex and others.

region	thickness			areal density		
0	0	–	–	0	–	–
1	2	mm	Al	0.54	g/cm^2	Al
2	30	mm	PMMA	3.6	g/cm^2	PMMA
3	2	mm	Al	0.54	g/cm^2	Al
	30	mm	PMMA	3.6	g/cm^2	PMMA
4	10	mm	PMMA	1.2	g/cm^2	PMMA
5	10	mm	PMMA	1.2	g/cm^2	PMMA
	20	mm	H_2O	2	g/cm^2	H_2O
	w/ 1.2	%	I	0.027	g/cm^2	I

Table 11.1 Thickness and areal density of the involved materials in the different regions of the phantom.

shows a picture of the setup with the Medipix2 detector visible in the background. The black square indicates the imaged region as it is seen on the detector.

The measurements were done with the Medipix2 detector with a 300 µm silicon sensor layer at 150 V bias voltage. The X-ray tube was operated at 50 kV with standard 1.4 mm Al filtering. The image in the counting regime can be seen in figure 11.2(b).

11.1.2 Application of Two Material Reconstruction Implementations

Two different implementations of the material reconstruction were applied. The first method includes two separate steps, first a pixel-wise spectrum reconstruction to compensate the energy response of the detector and than the actual material reconstruction step as introduced in 5.4.1.

The second method combines both steps into a maximum likelihood estimation (MLE) and does not need the explicit spectrum reconstruction. However, spectrum reconstruction is needed once to obtain the incident spectrum. This method was presented in section 5.4.4.

Both implementations of material reconstruction use PMMA, iodine and aluminum as basis materials here. This is the logical choice, since these are the only present materials in this setup. As PMMA and water show a similar attenuation spectrum, water will appear in the PMMA images.

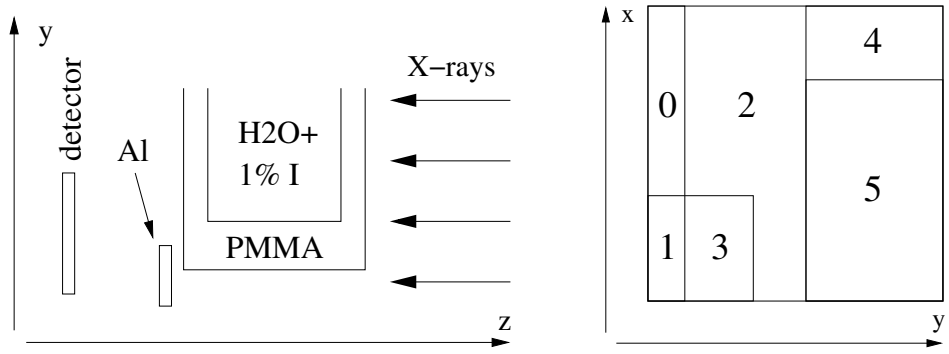

(a) y-z-plane (b) x-y-plane

Figure 11.1 Sketch of the radiography phantom from two views. (a) shows the view from top of the setup (y-z-plane) (b) shows the resulting regions as seen on the detector (x-y-plane).

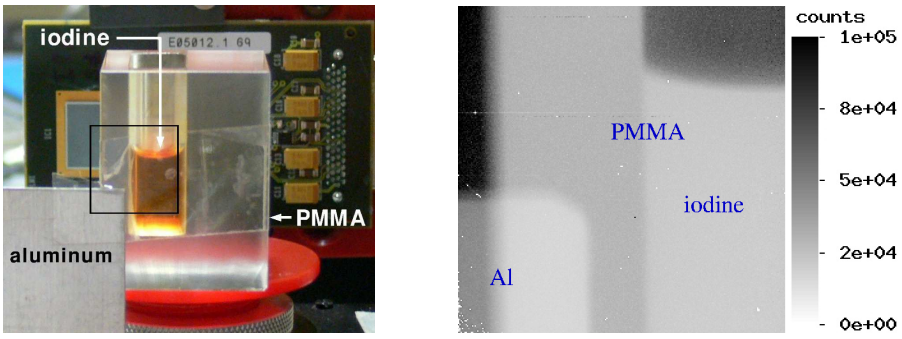

(a) photography (b) counting

Figure 11.2 (a) Photography of the setup. The black square indicates the region seen on the detector. (b) Photon counting X-ray image taken with the Medipix2 at 18.8 keV threshold

Two Step Method

Since the implementation of material reconstruction with prior spectrum stripping needs narrow energy channels, the images were acquired at 41 different thresholds, from 7.27 keV to 53.34 keV in steps of 1.152 keV. Spectrum reconstruction for each pixel was performed with 2 keV broad energy channels with central energies from 14 keV to 54 keV.

Material reconstruction through matrix inversion as described in 5.4.1 was applied with 15 energy samples obtained from the previous spectrum reconstruction. The samples used for the actual material reconstruction ranged from 20 to 48 keV central energy. The energy channels below 20 keV and above 48 keV were neglected, as they carry little information and only increase the dimension of the matrix.

The left column of figure 11.3 (a,c,e) shows the material reconstructed images of the basis materials PMMA, iodine and aluminum. They show that the method works very well. The single images represent the areal density of the respective basis material: The PMMA image shows the PMMA coverage, the iodine shows the iodine coverage and the aluminum image shows the aluminum coverage of the setup. However, there is some correlation between the material images. Especially in the aluminum images, "ghost"-images from PMMA are visible and vice versa. The increased noise level with unchanged mean value in regions 1 and 3 seen in the iodine image is due to decreased photon statistics. But more importantly, iodine can only be seen in the iodine image and does not appear in the aluminum or PMMA image.

Combined MLE Method

For the combined material reconstruction method, acquisitions were taken at only five different thresholds, but with the same current-time-product per acquisition as in the previous case. That leads to radiation dose of about one eighth. The energy thresholds of the Medipix2 detector were set to 18.8, 25.7, 32.6, 39.5 and 48.7 keV. To minimise the likelihood function, the MATLAB® built-in function `fminsearch` was used. This is an implementation of the Nelder-Mead-Simplex method [NM65, LRWW98]. The initial values for the areal densities were 1 g/cm^2 for PMMA, 0.1 g/cm^2 for aluminum and 0.01 g/cm^2 iodine.

The right column of figure 11.3 (b,d,f) shows the material reconstructed images resulting from the combination method. The separation of material works as well, but the correlation between the different material images is higher, especially regarding the aluminum component. The aluminum present in region 1 and 3 can not only be seen in the aluminum image, but also in the iodine and PMMA image.

The correlation between the material images is presumably due to scattered radi-

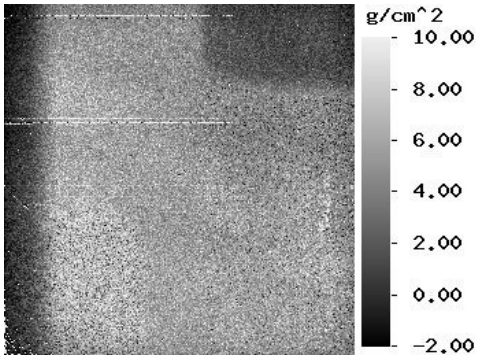

(a) Two step method. Material reconstructed areal density of PMMA

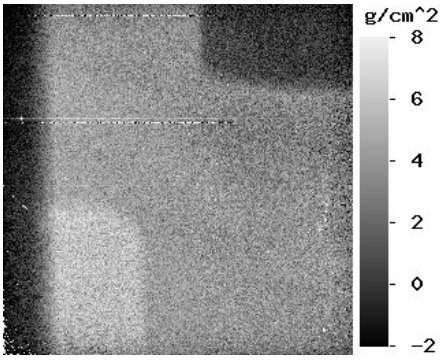

(b) Combination method. Material reconstructed areal density of PMMA

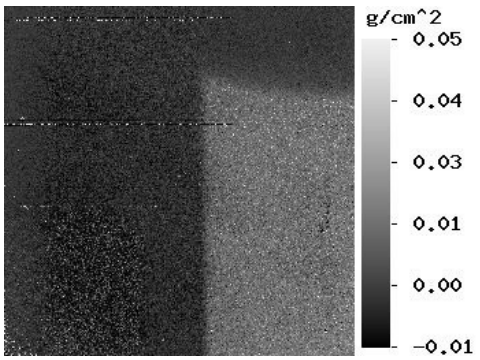

(c) Two step method. Material reconstructed areal density of iodine

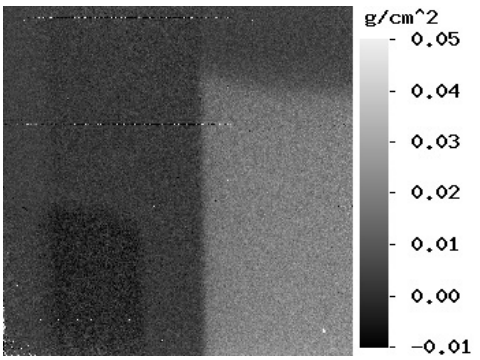

(d) Combination method. Material reconstructed areal density of iodine

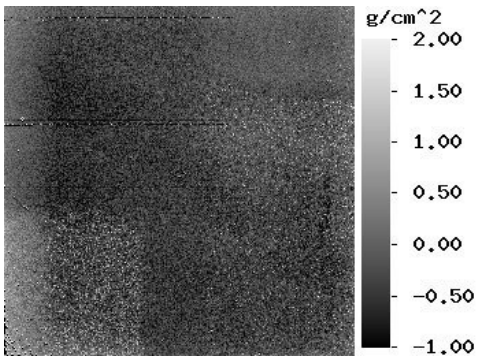

(e) Two step method. Material reconstructed areal density of aluminum

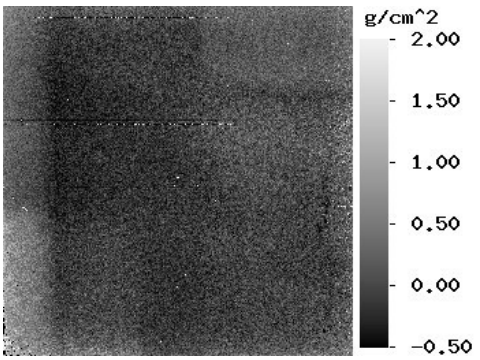

(f) Combination method. Material reconstructed areal density of aluminum

Figure 11.3 Comparison between two different material reconstruction implementations. In the left column, the method with spectrum reconstruction and subsequent material reconstruction by matrix inversion is shown. In the right column the images obtained through the combination method are shown.

ation. In material reconstruction, the total attenuation coefficient is used as basis. It therefore handles scattered radiation as no longer existent. If a scattered photon hits the detector, it yields a false contribution to the spectrum and the intensity. An anti-scatter grid could be used to reduce scattered radiation, but was not applied in this experiment.

11.2 Material Reconstruction in Computed Tomography

The material reconstruction method can also be applied in computed tomography (see section 5.5). In this case, it yields the volumetric partial density of the respective basis material.

11.2.1 Monte Carlo Simulations

To evaluate the theoretical performance of material reconstruction in computed tomography, Monte Carlo simulations were performed. Two different situations were simulated: in one case, the scattered radiation is suppressed by applying an optimal anti-scatter grid, the other one including the scattered radiation. An ideal detector with an ideal energy response was used to allow the evaluation of the method without any influence from the employed detector.

The Simulation Setup

The phantom for the simulation consists of a water cylinder containing four smaller cylinders. The main cylinder has a diameter on 20 cm. The four cylinders contain aqueous solution of the contrast agents iodine and gadolinium in different concentrations. They have a diameter of 5 cm. The concentrations of the contrast agents in the particular regions of phantom are itemised below and can be seen in figure 11.4(a).

region 1: Gadolinium $0.004\,\mathrm{g/cm^2}$

region 2: Iodine $0.002\,\mathrm{g/cm^2}$

region 3: Gadolinium and iodine, $0.002\,\mathrm{g/cm^2}$ each

region 4: Iodine $0.004\,\mathrm{g/cm^2}$

The CT scan was simulated over 360 degrees in steps of 1 degree. In each projection, $2.5 \cdot 10^8$ photons were simulated, altogether $9 \cdot 10^{10}$ photons. The energy of the photons was distributed according to an X-ray tube with tungsten anode operated at 120 kV with 0.6 mm titanium filtering. An ideal detector was employed, consisting of

256 detector elements arranged on a line 40 cm long. The photons impinging on the detector were sorted into four energy bins with borders at 50, 65 and 85 keV. The basis materials for the material reconstruction were water, iodine and gadolinium.

The simulation was done in a fan-beam geometry. In the coordinate system used, the detector and the source are fixed and the object is rotated. The central beam is along the z-axis and the 256 detector elements are arranged along the x-axis. For the evaluation of the impact of scattered radiation, the detector elements were enlarged in the y-direction, while the source remained in the fan-beam geometry. This has an impact on the ratio of scattered radiation S to primary radiation P. With the scattered radiation completely suppressed, the value of S/P is zero by definition. At the center, the detector enlargement in y direction results in a S/P of 0.256 for 5 cm, 0.479 for 10 cm and 0.932 for 20 cm.

Figure 11.4(b) shows the CT slice reconstructed from the counting mode data. Here, the energy information is not used, and the photons are summed over all energy bins. Scattered radiation is suppressed in this image. The CT slice is reconstructed by filtered back projection (FBP) on a 256×256 pixel matrix, using a soft $\left[\mathrm{abs}(k) \cdot \cos(k)\right]$-filter kernel. The regions containing contrast agents are clearly visible. However, it is not possible to distinguish between the different materials of the contrast agents.

Simulations Discriminating Scattered Radiation

In the simulations whith suppressed scattered photons, the material reconstruction works very precisely. The separation between the material is accurate, i. e. each material is visible only in its respective material image as can be seen in figure 11.7.

The material reconstruction method also provides quantitative information on the materials. The partial densities of the basis materials are reconstructed correctly. The water image yields the appropriate density for water ($1.0\,\mathrm{g/cm^3}$) as well as for the contrast agents (0.002 and $0.004\,\mathrm{g/cm^3}$ (see figure 11.4(a)).

Simulations Respecting Scattered Radiation

The influence of scattered radiation was evaluated in the simulation by taking into account the photons scattered out of the fan beam plane by up to 2.5 cm, 5 cm and 10 cm at the detector position. This corresponds to an increase of the height of the detector of 5 cm, 10 cm and 20 cm.

The CT slice images obtained from the counting mode acquisitions can be seen in figure 11.5. The line scans from row 93 of these images (just between region 1 and 2) is shown in figure 11.6. With increasing detector height, i. e. increasing amount

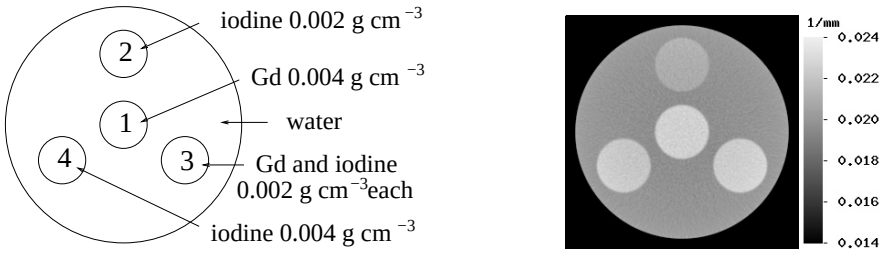

(a) Sketch of the phantom (b) Photon counting image

Figure 11.4 (a) Sketch of the simulation phantom with the densities of the contrast agents and (b) the resulting CT slice from the photon counting mode without scattered radiation.

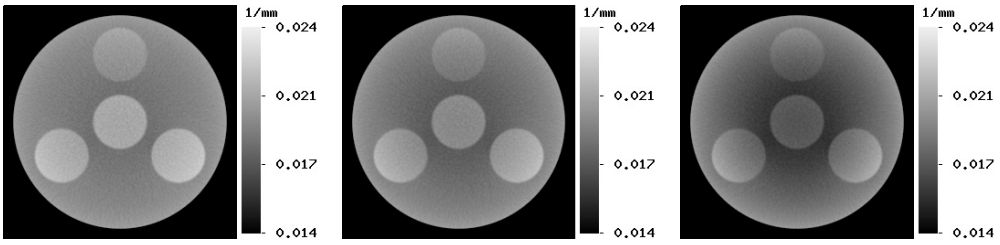

(a) 5 cm (b) 10 cm (c) 20 cm

Figure 11.5 CT slices reconstructed for the counting images for the different detector heights. The increased influence of scattering with increasing detector height can clearly be seen.

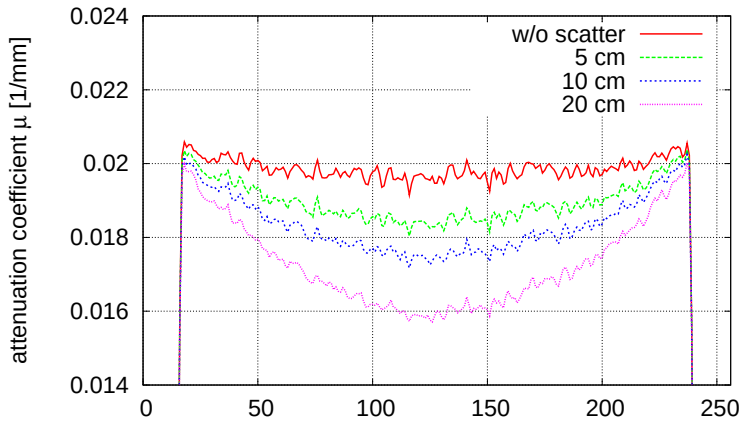

Figure 11.6 Linescans of row 93 (horizontal line between region 1 and 2) of the images in 11.5. Strong cupping artefacts can be seen.

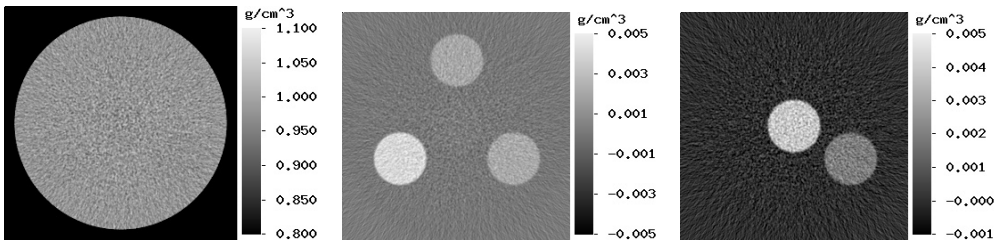

(a) water (b) iodine (c) gadolinium

Figure 11.7 Material reconstructed images without scattered radiation.

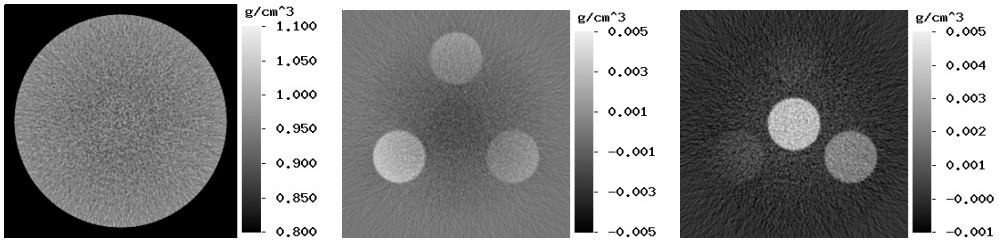

(a) water, 5 cm (b) iodine, 5 cm (c) gadolinium, 5 cm

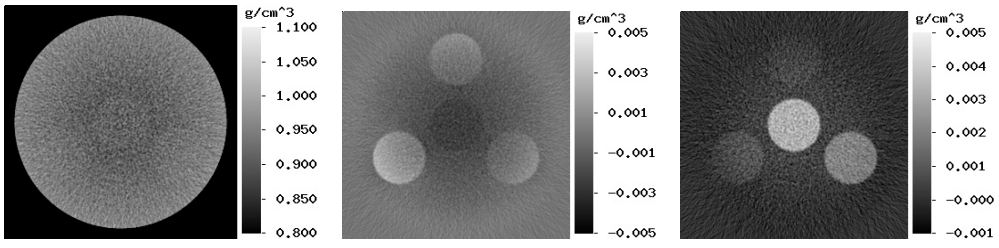

(d) water, 10 cm (e) iodine, 10 cm (f) gadolinium, 10 cm

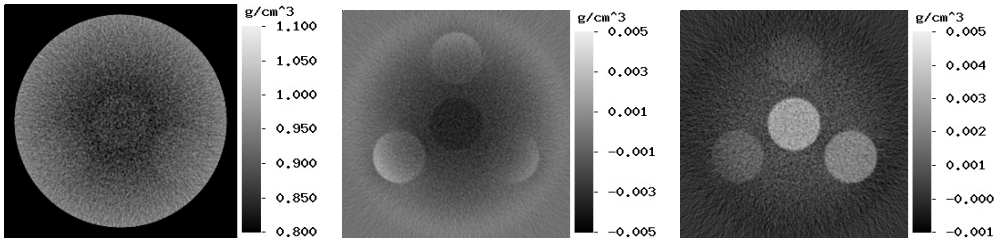

(g) water, 20 cm (h) iodine, 20 cm (i) gadolinium, 20 cm

Figure 11.8 The increasing effect of scattered radiation with enlarging the detector in y-direction. The images are captioned with the basis material and the detector height (y direction).

of scattered radiation detected, a cupping artefact becomes prominent. Cupping describes the reduced reconstructed attenuation coefficient in the central region due to beam hardening and scattered radiation. In the image with scattered radiation suppressed, the slight cupping is only due to beam hardening.

Besides cupping, the scattered radiation has an effect on material reconstruction. In the scatter-free material reconstructed images, the basis materials water, iodine and gadolinium are clearly separated, while in the images including an increasing amount of scattered radiation, not only the actual material is visible, but also one or more of the other materials. This becomes especially apperant with the iodine and the gadolinium images. In the gadolinium images, iodine appears, while in the iodine image, a negative image of the gadolinium image appears. This effect can clearly be seen in figure 11.7 and figure 11.8. The reason for this effect is that scattered radiation not only affects the total number of photon, but in the case of compton scattering also their energy.

The ability of the material reconstruction method to separate the basis materials is degraded severely by scattered radiation.

11.2.2 Measurements

The measurements for material reconstruction in computed tomography were carried out during a reaserch visit in spring 2008 at the University of Canterbury and the University of Otago medical school, both in Christchurch, New Zealand.

The subject of study was a 26.9 g male C57BL/6 mouse. It was anaesthetised by Ketamine (37.5 mg/kg) and Domitor (Medetomidine, 0.5 mg/kg) subcutaneously. It was prepared by the gavage of 0.8 ml iodine containing contrast agent solution (50% iohexol[2], 50% sterile water). Euthanasia was effected by intraperitoneal administration of sodium pentobarbital (0.5 ml/kg). Post mortem 0.4 ml gadopentetate dimeglumine[3] (gadolinium contrast agent) was injected into the chest. The work described was undertaken in accordance with University of Otago Animal Ethics regulations (approval number C8/07).

The CT scan of the mouse was done with the MARS scanner [BAT+08], using a Medipix2MXR with a 300 µm silicon sensor layer. The radiation source was an X-ray tube with a tungsten anode and a beryllium exit window. Additionally, the spectrum was filtered with 0.5 mm aluminum. The X-ray tube was operated at 74 kV.

[2]Omnipaque 350®, GE Healthcare AS, Oslo, Norway
[3]Magnevist®, Bayer Schering Pharma AG, Berlin, Germany

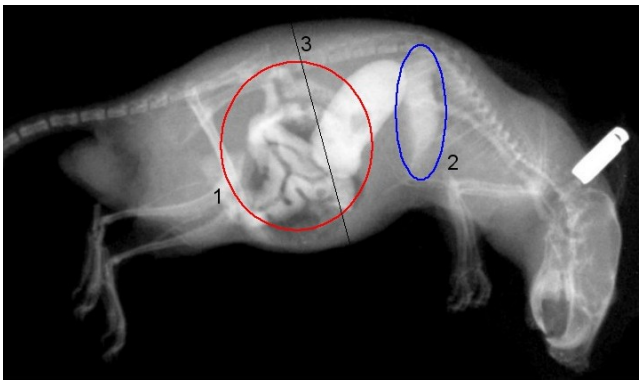

Figure 11.9 Plain radiograph of the prepared mouse. Thanks to Nigel Andeson for providing the image.

Due to the relatively small detector size, the detector was moved to three adjacent positions. The three resulting images per projection were tiled together afterwards, resulting in projections of 768×256 pixels. A full 360 degree scan was performed in steps of two degrees. The detector energy threshold was set to the values 12, 17, 33, 42 keV. The acquisition times at a tube current of 80 µA were 1 s for the 12 keV threshold, 2 s for the 17 keV threshold, 5 s for the 33 keV threshold and 8 s for the 42 keV threshold at each detector position. The CT reconstruction of the data were done using the Octopus software developed by UGCT, University Gent in collaboration with the MARS group in Christchurch.

The threshold equalisation of the Medipix2 detector was not done at the electronic noise edge as usual, but with flat field images obtained under radiation [Nie06]. The detector energy threshold was set to energy of the K-edge of iodine (33 keV) to provide highest accuracy in this energy range.

The plain radiograph shown in figure 11.9 shows the mouse after the gavage of the contrast agent. Clearly visible is the iodinated contrast within the bowel (red circle number 1), in the stomach (the bright oval object between 1 and 2, partly inside 1) and the gadolinium in the pleural space (blue circle number 2). The black line (number 3) shows the position of the CT slice shown in figure 11.10. It is just an approximate position, as the actual CT-scan was taken with the mouse inside a PMMA tube. The gadolinium is not in the field of view of the CT images.

The CT images corresponding to the different threshold energies of the detector can be seen in 11.10(a)–(d). The iodine contrast agent can be seen in all four images.

In the images with the detection energy threshold at 12 keV and 17 keV, the iodine shows about the same attenuation as the vertebral body in the upper right region.

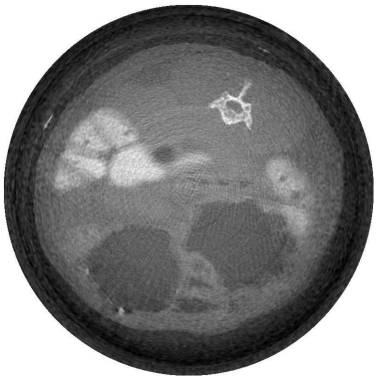

(a) threshold at 12 keV

(b) threshold at 17 keV

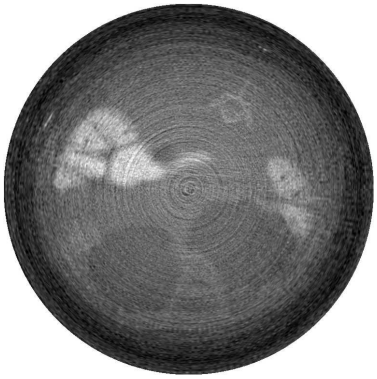

(c) threshold at 33 keV

(d) threshold at 42 keV

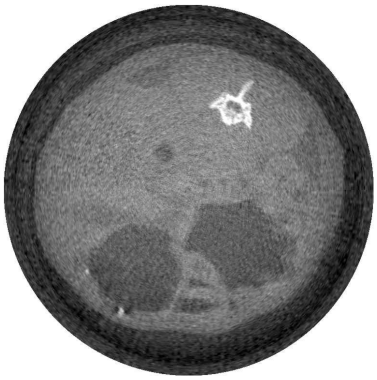

(e) Material reconstruction: water image

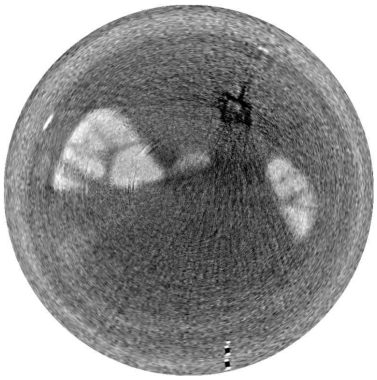

(f) Material reconstruction: iodine image

Figure 11.10 (a)–(d) CT reconstructed images for the four different energy thresholds at 12, 17, 33 and 42 keV; (e)–(f) the material reconstructed images using the basis materials water and iodine.

At 33 keV energy threshold, the higher absorption due to the iodine K-edge at that energy can be seen.

For the material reconstruction, the projections were rescaled to 384×128 pixels to reduce computation time. The combination method for material reconstruction (see section 5.4.4) was used. The material reconstruction for one projection took approximately 90 minutes on a current PC (2.4 GHz Intel core2® CPU, 1GB RAM).

Material reconstruction was applied using water and iodine as basis materials, as water is the main constituent of the biological object and the iodine contrast agent is the material of the actual interest. The material images can be seen in 11.10(e)–(f). The separation of iodine from soft tissue (mostly water) and bone is clearly visible. The bone of the vertebral body is visible in the water image as the energy dependence of the attenuation coefficient of bone is closer to water's that to iodine's. This is due to the iodine K-edge at 33.2 keV, which provides a significant property. As a result, the water image shows all tissue including bone and no iodine at all. The iodine image shows the iodine content exclusively and no soft tissue. However, the iodine image also shows a negative image of the bone. This is presumably due to scattered radiation, as no anti-scatter grid was applied. Although being an artefact, this effect actually helps to distinguish the iodine contrast agents from other high contrast contents of the image.

11.3 Conclusion

In this chapter, the application of the material reconstruction method in both a radiography setup and in computed tomography has been presented. Measurements and Monte Carlo simulations have been carried out. The method allows the quantitative reconstruction of the areal density (radiography) and the volumetric partial density (CT) of the employed basis materials, but is sensitive to accurate detector calibration. The impact of scattered radiation has been studied using a Monte Carlo simulation. Scattered radiation strongly influences the method and needs further investigation.

The material reconstruction method was successfully applied to a CT scan of a mouse with iodine contrast agent. In the resulting material images, the iodine contrast agent can clearly be distinguished from soft tissue and bone.

Summary

In this thesis a method was developed and successfully tested to reconstruct the concentration and distribution of elements or basis materials in an object through energy resolving detection of X-rays. This method of material reconstruction relies on the difference in the energy dependence of the attenuation coefficients of the basis materials. The photon counting pixel detector Medipix2 was used.

To achive this goal, the energy resolving properties of the Medipix2 were evaluated. A monochromator was set up and the energy response of the detector system to monochromatic irradiation was studied. The effects dominating the energy response behaviour of the detector were successfully modeled in a Monte Carlo simulation which could reproduce the measurements. A complete set of energy response functions of the detector could be simulated in the relevant energy range.

The knowlege of these energy response functions of the detector allowed the development of the spectrum reconstruction. This technique provides the actual spectrum impinging on the detector for every pixel from the distorted measured spectrum through a deconvolution. Two different implemetations of the technique were compared. Multiple X-ray spectra were measured with the Medipix2 and reconstructed successfully with this method.

Different variants of the material recontrution technique were developed. One approach includes an initial spectrum recontruction and a subsequent algebraic material reconstruction step, an other is to calculate the likelihood of a particular combination of basis material concentrations to yield a given measurement and perform a maximum likelihood estimation.

Measurements in a radiography setup with a phantom containing PMMA, aluminum and iodine were done using the Medipix2 detector at different energy thresholds. Material reconstruction was successfully applied with the basis materials PMMA, aluminum and iodine. The resulting material specific images were shown.

The Method was transferred to computed tomography. Monte Carlo simulation were carried out to investigate the quantitative features of the method and the influence of scattered radiation to the method. A CT scan of a mouse with contrast agent iodine was performed. Material Reconstruction was conducted with the basis material water and iodine. The resulting material specific images show that the material reconstruction works very well.

Furthermore, a method to enlarge the field of view in computed tomography was developed. It is an extension of the sinogram reflection technique and is particularly suitable for two or more small detectors. Measurements and Monte Carlo simulations were done to verify the method.

Zusammenfassung

In dieser Arbeit wurde eine Methode zur Rekonstruktion der Konzentration und der Verteilung von Elementen oder Basismaterialien mittels Röntgenstrahlung entwickelt und erfolgreich getestet. Diese hier vorgestellte Methode der Materialrekonstruktion beruht auf der unterschiedlichen Energieabhängigkeit der Schwächungskoeffizienten der verwendeten Basismaterialien. In Experimenten hierzu wurde der photonenzählende Röntgendetektor Medipix2 verwendet.

Um dies zu erreichen, wurden die Energieauflösungseigenschaften des Medipix2-Detektors untersucht. Zur Messung der Detektorantwort bezüglich der Energie bei monochromatischer Bestrahlung wurde ein einfacher Monochromator aufgebaut. Die Effekte, die diese Energieantwort bestimmen, konnten identifiziert und in eine Monte-Carlo-Simulation, welche die Messergebnisse sehr gut reproduziert, implementiert werden. Dadurch konnte für alle erwünschten Energien die Detektorantwort simuliert werden.

Die Kenntnis dieser Energieantwortfunktionen erlaubte die Entwicklung einer Methode zur Spektrumsrekonstruktion. Diese liefert durch eine Rückfaltung das in jedem Pixel des Detektor einfallende Spektrum aus dem verändertem Spektrum, das die Messung mit einem Detektor wie dem Medipix2 liefert. Es wurden mehrere Röntgenspektren gemessen und zwei verschiedene Implementierungen der Spektrumsrekonstruktion angewendet und verglichen.

Verschiedene Varianten der Materialrekonstruktion wurden entwickelt. Ein Ansatz beinhaltet als ersten Schritt eine Spektrumsrekonstruktion und anschließend den Materialrekonstruktionsschritt. Bei einem zweiten Ansatz wird die Likelihood-Funktion aufgestellt und durch eine Maximum-Likelihood-Schätzung die wahrscheinlichste Kombination von Basismaterialkonzentrationen bestimmt, die zu diesem Messergebnis führt.

Mit einem Phantom aus PMMA[4], Jodlösung und Aluminium wurden Messungen in projektiver Geometrie mit dem Medipix2-Detektor bei verschiedenen Energieschwellen durchgeführt. Die Materialrekonstruktion mit den Basismaterialien PMMA, Aluminium und Jod konnte erfolgreich angewendet werden. Die resultierenden materialspezifischen Bilder wurden vorgestellt.

[4]Polymethylmethacrylat, Handelsname Plexiglas®

Die Methode der Materialrekonstruktion wurde erfolgreich auf die Computertomographie übertragen. Es wurden Monte-Carlo-Simulationen zur Untersuchung der quantitativen Eigenschaften der Methode und des Einflusses von Streustrahlung durchgeführt. Eine Kontrastmittel-CT-Aufnahme einer Maus mit dem Medipix2 als Detektor wurde erstellt und die Materialrekonstruktion mit Wasser und Jod als Basismaterialien erfolgreich angewendet. Die resultierenden materialspezifischen Bilder zeigen, dass die Methode sehr gut funktioniert.

Außerdem wurde auf Basis der Sinogrammreflektion eine Methode zur Vergrößerung des Sichtfelds in der Computertomographie entwickelt, die sich besonders für zwei und mehr kleine Detektoren eignet. Die Methode konnte sowohl in der Simulation als auch in der Messung verifiziert werden.

Bibliography

[ABB+93] W. Atwood, A. Breakstone, D. Britton, T. Burnett, D. Myers, and G. Word. The GISMO Project (C++). *C++ Report*, 5(3):38–43, 1993.

[ABS80] R. C. Alig, S. Bloom, and C. W. Struck. Scattering by ionization and phonon emission in semiconductors. *Phys. Rev. B*, 22(12):5565–5582, Dec 1980.

[ACD+06] A. Averbuch, R.R. Coifman, D.L. Donoho, M. Elad, and M. Israeli. Fast and accurate Polar Fourier transform. *Applied and Computational Harmonic Analysis*, 21(2):145–167, September 2006.

[BAT+08] A.P.H. Butler, N.G. Anderson, R. Tipples, N. Cook, R. Watts, J. Meyer, A.J. Bell, T.R. Melzer, and P.H. Butler. Bio-medical X-ray imaging with spectroscopic pixel detectors. *Nuclear Instruments and Methods in Physics Research Section A: Accelerators, Spectrometers, Detectors and Associated Equipment*, 591(1):141 – 146, 2008. Radiation Imaging Detectors 2007 - Proceedings of the 9th International Workshop on Radiation Imaging Detectors.

[BBD+08] M. Bech, O. Bunk, C. David, P. Kraft, C. Bronnimann, E.F. Eikenberry, and F. Pfeiffer. X-ray imaging with the PILATUS 100k detector. *Applied Radiation and Isotopes*, 66(4):474–478, 2008.

[BCH+07] R. Ballabriga, M. Campbell, E.H.M. Heijne, X. Llopart, and L. Tlustos. The Medipix3 Prototype, a Pixel Readout Chip Working in Single Photon Counting Mode With Improved Spectrometric Performance. *IEEE Trans. Nucl. Sci.*, 54(5):1824–1829, Oct. 2007.

[BDV94] G.D. Burns, R.B. Daoud, and J.R. Vaigl. LAM: an open cluster enviroment for MPI. Technical report, Supercomputung Symposium, 1994.

[BFJ97] J.M. Boone, T.R. Fewell, and R.J. Jennigs. Molybdenum, rhodium and tungsten anode spectral models using interpolating polynomials with application to mammography. *Med. Phys.*, 24(12):1863–1874, 1997.

[BHea98] M. J. Berger, J.H. Hubbell, and S.M. Seltze et al. XCOM: Photon Cross Sections Database, NIST Standard Reference Database. available online `http://physics.nist.gov/PhysRefData/Xcom/Text/XCOM.html`, 1998.

[BL98] V. Blobel and E. Lohrman. *Statistische und numerische Methoden der Datenanalyse*. Teubner Studienbücher, 1998.

[BS97] J.M. Boone and J.A. Seibert. An accurate method for computer-generating tungsten anode x-ray spectra from 30 to 140kV. *Med. Phys.*, 24(11):1661–1670, 1997.

[BvBJ+03] D. San Segundo Bello, M. van Beuzekom, P. Jansweijer, H. Verkooijen, and J. Visschers. An interface board for the control and data acquisition of the Medipix2 chip. *Nucl. Instr. and Meth. A*, 509(1–3):164–170, August 2003.

[CHM+98] M. Campbell, E.H.M. Heijne, G. Meddeler, E. Pernigotti, and W. Snoeys. Readout for a 64 x 64 pixel matrix with 15-bit single photon counting. *IEEE Trans. Nucl. Sci.*, 45(3):751–753, June 1998.

[Cor63] A. M. Cormack. Representation of a Function by Its Line Integrals, with Some Radiological Applications. *Journal of Applied Physics*, 34(9):2722–2727, 1963.

[Dur08] J. Durst. *Modellierung und Simulation physikalischer Eigenschaften photonenzählender Röntgenpixeldetektoren für die Bildgebung*. PhD thesis, University of Erlangen-Nürnberg, Germany, July 2008.

[EBB+04] F. Edling, N. Bingefors, R. Brenner, K. Fransson, L. Gustafsson, L. del Risco Norrlid, and C. Rönnqvist. Characterisation of a pixel readout chip for medical X-ray imaging. *Nucl. Instr. and Meth. A*, 525:217–220, June 2004.

[Fan47] U. Fano. Ionization Yield of Radiations. II. The Fluctuations of the Number of Ions. *Phys. Rev.*, 72(1):26–29, Jul 1947.

[FHO+98] P. Fischer, J. Hausmann, M. Overdick, B. Raith, N. Wermes, L. Blanquart, V. Bonzom, and P. Delpierre. A counting pixel readout chip for imaging applications. *Nucl. Instr. and Meth. A*, 405(1):53 – 59, 1998.

[Fou91] Free Software Foundation. GNU Public Licence (GPL). available online `http://www.gnu.org/licenses/gpl.html`, 1991. Version 2.

[GD08] Jürgen Giersch and Jürgen Durst. Monte Carlo simulations in X-ray imaging. *Nuclear Instruments and Methods in Physics Research Section A: Accelerators, Spectrometers, Detectors and Associated Equipment*, 591(1):300 – 305, 2008. Radiation Imaging Detectors 2007 - Proceedings of the 9th International Workshop on Radiation Imaging Detectors.

[Gie02] J. Giersch. *Photonenzählende Pixel-Röntgendetektoren*. PhD thesis, Friedrich-Alexander-Universität Erlangen-Nürnberg, 2002.

[Gie04] J. Giersch. ROentgenSImulation ROSI. available online `http://www.pi4.physik.uni-erlangen.de/Giersch/ROSI/index.html`, 2004.

[GWA03] J. Giersch, A. Weidemann, and G. Anton. ROSI – an object-oriented and parallel-computing Monte Carlo simulation for X-ray imaging. *Nucl. Instr. and Meth. A*, 509:151–156, 2003.

[GWA04] J. Giersch, A. Weidemann, and G. Anton, editors. *LSCAT-GISMO - an object-orientated Framework for Particle Simulation*, 2004. 3rd International EGS Workshop, KEK, Japan.

[HJP+06] T. Holy, J. Jakubek, S. Pospisila, J. Uher, D. Vavrik, and Z. Vykydal. Data acquisition and processing software package for Medipix2. *Nucl. Instr. and Meth. A*, 563:254–258, 2006.

[Hou73] G.N. Hounsfield. Computerized transverse axial scanning (tomography). Part I: Description of system. Part II: Clinical applications. *British Journal of Radiology*, 46:1016–1022, 1973.

[ICR89] ICRU Report. *Tissue Substitutes in Radiation Dosimetry and Measurement*, volume 44. International Commission on Radiation Units and Measurements, 1989.

[ICR92] ICRU Report. *Photon, Electron, Proton and Neutron Interaction Data for Body Tissues*, volume 46. International Commission on Radiation Units and Measurements, 1992.

[Jam90] F. James. A review of pseudorandom number generators. *Computer Physics Communications*, 60:329–344, 1990.

[KFS87] W. Kalender, D. Felsenberg, and C. Süss. Material selective imaging and density measurement with the dual energy method. III. Determination of bone mineral of the spine with CT. *Digitale Bilddiagn*, 7(4):170–176, Dec 1987.

[Kor07] A. Korn. *Spektrale und bildgebende Eigenschaften photonenzählender Röntgendetektoren am Beispiel des Medipix-Detektors.* PhD thesis, Friedrich-Alexander Universität Erlangen-Nürnberg, 2007.

[Kre06] B. Kreisler. Influenzierte Signale in pixelierten Halbleiter-Röntgen-Detektoren. Master's thesis, Universität Erlangen-Nürnberg, 2006.

[KVS00] A.R. Kalukin, M. Van Geet, and R. Swennen. Principal Components Analysis of Multienergy X-Ray Computed Tomography of Mineral Samples. *IEEE Trans. Nucl. Sci.*, 47(5):1729–1736, 2000.

[LCD+02] X. Llopart, M. Campbell, R. Dinapoli, D. San Segundo, and E. Pernigotti. Medipix2: A 64-k pixel readout chip with 55-μm square elements working in single photon counting mode. *IEEE Trans. Nucl. Sci.*, 49(5):2279–2283, 2002.

[LFK+04] M. Locker, P. Fischer, S. Krimmel, H. Kruger, M. Lindner, K. Nakazawa, T. Takahashi, and N. Wermes. Single photon counting X-ray imaging with Si and CdTe single chip pixel detectors and multichip pixel modules. *Nuclear Science, IEEE Transactions on*, 51(4):1717–1723, Aug. 2004.

[Llo07] X. Llopart. *Design and Characterization of 64K Pixels Chips Working in Single Photon Processing Mode.* PhD thesis, Mid Sweden University, 2007.

[LRWW98] J. Lagarias, J. Reeds, M. Wright, and P. Wright. Convergence Properties of the Nelder-Mead Simplex Method in Low Dimensions. *SIAM Journal of Optimization*, 9:112–147, 1998.

[Med] Medipix2 Collaboration. `http://medipix.web.cern.ch/MEDIPIX/`.

[MSJ04] T. Menezes, P.J. Sellin, and P.M. Jenneson. Characterisation of a multiple-line fluorescence X-ray tube for security imaging applications. *Nucl. Instr. and Meth. A*, 525:342–345, June 2004.

[NBC+79] M. Nassi, W. R. Brody, P. R. Cipriano, P. Stonestrom, C. Morehouse, D. Moss, and A. Macovski. Applicatiobn of a reflection technique for improved temporal resolution with dynamic and ECG-gated computed tomography. *Proc. SPIE 206*, 1:103–108, 1979.

[NDHB02] H. E. Nilsson, E. Dubaric, M. Hjelm, and K. Bertilsson. Simulation of photon and charge transport in X-ray imaging semiconductor sensors. *Nucl. Instr. and Meth. A*, 487(1-2):151–162, July 2002.

[NH00] Y. Namito and H. Hirayama. LSCAT: Low-Energy Photon-Scattering Expansion for the EGS4 Code (Inclusion of Electron Impact Ionization). Technical report, High Energy Accelerator Research Organization, Japan, May 2000.

[NHR85] W.R. Nelson, H. Hirayama, and D.W.O. Rogers. The EGS4 Code System. Technical report, Standford Linear Accelerator Center SLAC-265, 1985.

[Nie06] Daniel Niederlöhner. *Untersuchung zur Energiewichtung in der medizinischen Bildgebung mit dem Medipix2-Detektor*. PhD thesis, Friedrich-Alexander Universität Erlangen-Nürnberg, 2006.

[NM65] J.A. Nelder and R. Mead. A simplex method for function minimization. *The Computer Journal*, 7(4):308–313, 1965.

[Opp05] A. Oppelt, editor. *Imaging Systems for Medical Diagnostics*. Publics Corporate Publishing, Erlangen, 2005.

[PBB+07] P. Pangaud, S. Basolo, N. Boudet, J.-F. Berar, B. Chantepie, P. Delpierre, B. Dinkespiler, S. Hustache, M. Menouni, and C. Morel. XPAD3: A new photon counting chip for X-ray CT-scanner. *Nucl. Instr. and Meth. A*, 571(1-2):321–324, February 2007.

[Pfe04] K.-F.G. Pfeiffer. *Evaluation of the Medipix Detectors for Medical X-Ray Imaging, with Special Consideration of Mammography*. PhD thesis, Friedrich-Alexander-Universität Erlangen-Nürnberg, 2004.

[PJH] S. Pospisil, J. Jakubek, and T. Holy. Medipix in IEAP (Institute of Technical and Experimental Physics CTU in Prague). available online `http://aladdin.utef.cvut.cz/ofat/index.html`.

[Pon08] C. Ponchut. Correction of the Charge Sharing in Photon-Counting Pixel Detector Data. *Nucl. Instr. and Meth. A*, 591(1):311–313, 2008.

[Rad17] J.H. Radon. Über die Bestimmung von Funktionen durch ihre Integralwerte längs gewisser Mannigfaltigkeiten. In *Ber. vor Sächs. Akad. Wiss.*, 1917.

[SBE+04] B. Schmitt, Ch. Brönnimann, E.F. Eikenberry, G. Hülsen, H. Toyokawa, R. Horisberger, F. Gozzo, B. Patterson, C. Schulze-Briese, and T. Tomizaki. Development of single photon counting detectors at the Swiss Light Source. *Nucl. Instr. and Meth. A*, 518:436–439, 2004.

[SH85] H. G. Spieler and E. E. Haller. Assessment of Present and Future Large-Scale Semiconductor Detector Systems. *IEEE Transactions on Nuclear Science*, NS-32(1):419–426, February 1985.

[Tlu05] L. Tlustos. *Performance and limitations of high granularity single photon processing X-ray imaging detectors.* PhD thesis, University of Technology, Vienna, 2005. CERN-THESIS-2005-032.

[Vyk05] Z. Vykydal. Microprocessor controlled USB interface for Medipix2 detector. Master's thesis, Czech Technical University in Prague, 2005.

[ZTS05] A. A. Zamyatin, K. Taguchi, and M. D. Silver. Helical cone beam CT with an asymmetrical detector. *Medical Physics*, 32(10):3117–3127, 2005.

Acknowledgements

At this point, I would like to express my gratitude to all the people who contributed, directly or indirectly, to this work. I can not name all of them and hope no one feels left out.

First, let me thank Prof. Gisela Anton for providing the opportunity to realise this work. She gave me a free hand for my research while always offering her advice when needed. I would like to thank the novel detectors group, especially my colleagues from room 213 Björn Kreisler and and Frank Nachtrab, for creating a great atmosphere. They did not only provide valuable scientific discussions and feedback, but also social activities.

Furthermore, I owe thanks to the Medipix2 collaboration, especially to the groups in Prague and at CERN who always had an open ear for my questions and problems. Parts of the results presented here were obtained during a research visit in Christchurch, New Zealand. Thanks to the complete MARS team for all the support and making this visit a success. Thanks to Kati Kania and Anthony Butler for proofreading the manuscript.

I would like to thank my entire family, particulary my parents Irmgard and Wolfgang, who always supported and encouraged me. None of this would have been possible without them. Finally, I would like to thank Karolin. I do not know where to start nor where to end – just for everything.